6-4-2018

Mountain-Wave Propagation under Transient Tropospheric Forcing: A DEEPWAVE Case Study

Tanja C. Portele
Deutsches Zentrum für Luft- und Raumfahrt

Andreas Dörnbrack
Deutsches Zentrum für Luft- und Raumfahrt

Johannes S. Wagner
Deutsches Zentrum für Luft- und Raumfahrt

Sonja Gisinger
Deutsches Zentrum für Luft- und Raumfahrt

Benedikt Ehard
Deutsches Zentrum für Luft- und Raumfahrt

Pierre-Dominique Pautet
Utah State University, dominiquepautet@gmail.com

Recommended Citation

Portele, T.C., A. Dörnbrack, J.S. Wagner, S. Gisinger, B. Ehard, P. Pautet, and M. Rapp, 2018: Mountain-Wave Propagation under Transient Tropospheric Forcing: A DEEPWAVE Case Study. Mon. Wea. Rev., 146, 1861–1888, https://doi.org/10.1175/MWR-D-17-0080.1

Mountain-Wave Propagation under Transient Tropospheric Forcing: A DEEPWAVE Case Study

TANJA C. PORTELE, ANDREAS DÖRNBRACK, JOHANNES S. WAGNER, SONJA GISINGER, BENEDIKT EHARD, PIERRE-DOMINIQUE PAUTET,[a] AND MARKUS RAPP

Institut für Physik der Atmosphäre, Deutsches Zentrum für Luft- und Raumfahrt, Oberpfaffenhofen, Germany

(Manuscript received 27 March 2017, in final form 14 January 2018)

ABSTRACT

The impact of transient tropospheric forcing on the deep vertical mountain-wave propagation is investigated by a unique combination of in situ and remote sensing observations and numerical modeling. The temporal evolution of the upstream low-level wind follows approximately a $\cos^2$ shape and was controlled by a migrating trough and connected fronts. Our case study reveals the importance of the time-varying propagation conditions in the upper troposphere and lower stratosphere (UTLS). Upper-tropospheric stability, the wind profile, and the tropopause strength affected the observed and simulated wave response in the UTLS. Leg-integrated along-track momentum fluxes ($-\mathrm{MF}_{\mathrm{track}}$) and amplitudes of vertical displacements of air parcels in the UTLS reached up to 130 kN m^{-1} and 1500 m, respectively. Their maxima were phase shifted to the maximum low-level forcing by ≈8 h. Small-scale waves ($\lambda_x \approx 20 - 30$ km) were continuously forced, and their flux values depended on wave attenuation by breaking and reflection in the UTLS region. Only maximum flow over the envelope of the mountain range favored the excitation of longer waves that propagated deeply into the mesosphere. Their long propagation time caused a retarded enhancement of observed mesospheric gravity wave activity about 12–15 h after their observation in the UTLS. For the UTLS, we further compared observed and simulated $\mathrm{MF}_{\mathrm{track}}$ with fluxes of 2D quasi-steady runs. UTLS momentum fluxes seem to be reproducible by individual quasi-steady 2D runs, except for the flux enhancement during the early decelerating forcing phase.

1. Introduction

Mountain waves under transient tropospheric forcing conditions were frequently observed during the Deep Propagating Gravity Wave Experiment (DEEPWAVE) in austral winter 2014 (Fritts et al. 2016). These events occurred episodically and were associated with migratory low pressure systems impinging the South Island (SI) of New Zealand (NZ; Gisinger et al. 2017). During these events, the conditions for wave excitation and propagation varied temporally. Continuous ground-based lidar observations in the lee of New Zealand's Alps during DEEPWAVE revealed enhanced gravity wave activity in the stratosphere and mesosphere, which lasted about 1–3 days and alternated with quiescent periods (Kaifler et al. 2015). The gravity wave forcing due to passing weather systems, the appearance of tropopause jets, and the middle atmosphere wave response were all observed with a similar frequency and duration of 2–4 days (Fritts et al. 2016; Gisinger et al. 2017).

The episodic nature of mountain wave events due to traversing cyclones was already observed during the Mesoscale Alpine Programme (MAP) and the Terrain-Induced Rotor Experiment (T-REX; Smith et al. 2007; Grubišić et al. 2008; Strauss et al. 2016). During T-REX, the transient formation of rotors and lee waves was investigated (Kühnlein et al. 2013), as well as the onset of downslope wind storms with shifting wave patterns aloft (Strauss et al. 2016). During both field campaigns, the observations focused on processes within the troposphere, including the boundary layer. Deep propagation of mountain waves was almost impossible during MAP, as directional wind shear in the midtroposphere acted like a critical level, except for above the western Alpine arc (Smith et al. 2007).

The design of DEEPWAVE allowed, inter alia, to measure orographically induced gravity waves from their excitation over the mountains of the Southern Alps

[a] Current affiliation: Center for Atmospheric and Space Sciences, Utah State University, Logan, Utah.

Corresponding author: Tanja C. Portele, tanja.portele@dlr.de

DOI: 10.1175/MWR-D-17-0080.1

up to their dissipation in the middle atmosphere (Fritts et al. 2016; Bramberger et al. 2017). The SI of NZ is located at about 45°S, just between the polar front jet to the south and the subtropical jet to the north. The frequent appearance of frontal systems allows one to study the transient forcing conditions for mountain-wave excitation and their impact on the gravity wave activity in the middle atmosphere. The nearly unidirectional westerly winds from the troposphere to the stratosphere during austral winter are strong enough that total critical levels are unlikely (Kim et al. 2003; Fritts et al. 2016). For an inviscid, adiabatic, nonrotating, steady, Boussinesq flow across mountains, linear theory gives total critical levels whenever the scalar product of horizontal wind (u, v) and horizontal wave vector (k, l) is zero for all wavenumbers (Teixeira 2014). Thus, the DEEPWAVE campaign offered the opportunity to study transient tropospheric forcing and the corresponding deep atmospheric wave response for the first time.

The steady-state assumption is the basis of linear mountain-wave theory (Smith 1979). Moreover, there are numerous numerical studies about transiently forced mountain waves. Lott and Teitelbaum (1993a,b) investigated the wave dynamics in a 2D linear time-dependent model with transient incident stably stratified flow. Chen et al. (2005, 2007) and Hills and Durran (2012) extended the work of Lott and Teitelbaum (1993a,b) and studied the impact of the flow of a time-dependent barotropic planetary square wave in a uniformly stratified atmosphere over an isolated 3D mountain in idealized numerical simulations. Martin and Lott (2007) further addressed the large-scale effect of inertia–gravity wave generation due to the passage of an idealized front over a 3D mountain range. Recently, Menchaca and Durran (2017) simulated an idealized cyclone passing an isolated ridge in a baroclinically unstable environment and investigated the wave structures and the flow morphologies in the course of the idealized event. Lott and Teitelbaum (1993a,b), as well as Chen et al. (2005, 2007) and Hills and Durran (2012), prescribed the cross-mountain wind variation during 2 and up to 8 days with cosine functions, increasing the wind from zero to a maximum of $20\,\mathrm{m\,s^{-1}}$ and returning to zero afterward. With such a time-varying incident flow, hydrostatic wave perturbations no longer appeared over the mountains, but were shifted downstream or upstream under accelerating or decelerating forcings, respectively. For low mountains, wave momentum flux was accumulated during accelerating forcing due to conservation of wave action. In contrast, the flow over higher mountains generated gravity wave breaking at lower levels. Here, the accumulated maximum of the zonal momentum flux during the high-drag state occurred shortly after the time of maximum wind.

So far, no real-world case studies exist investigating a mountain-wave field excited by transient low-level forcing and propagating into the middle atmosphere. In this case study, a mountain-wave event that occurred in the period of 28 June–1 July 2014 [intensive observing period (IOP) 9] is investigated. The overall questions are as follows:

1) Which tropospheric and stratospheric quantities control the transience of the event?
2) How do flux values, wave amplitudes, and wave scales in the upper troposphere and lower stratosphere (UTLS) respond to the varying conditions?
3) Does the transient tropospheric forcing favor the excitation of certain horizontal wavelengths?
4) Can the wave response in the UTLS be described by a sequence of individual steady states?
5) How does the transient low-level forcing affect the wave activity in the mesosphere?

The paper is structured as follows. First, a description of the used dataset and the applied methods is given in section 2. The following section 3 provides a detailed description of the meteorological evolution during IOP 9. The results are presented separately for the wave response in the UTLS (section 4a) and for the deep vertical wave propagation into the mesosphere (section 4b). The findings are discussed and related to literature in section 5. The research questions are answered in section 6. The appendix gives an overview of the extended wavelet transform used in this paper.

2. Methodology

IOP 9 took place from 28 June to 1 July 2014. Altogether, six coordinated flights of the NSF/NCAR Gulfstream V (GV; RF11–RF14) and the DLR research aircraft Falcon (FF01 and FF02) were conducted. During IOP 9, different flight patterns were flown (Fig. 1). Flight altitudes and times can be extracted from Fig. 2.

The analysis presented in this paper focuses on observations along the Mt. Aspiring 2b (hereinafter Mt-A-2b) transect (Fig. 1), a mountain-wave flight track with a direction of 300° from northwest to southeast over Mt. Aspiring (44.38°S, 168.73°E). During IOP 9, a total flight duration of 9.5 h was spent along this transect comprising 19 flight legs (RF12: six legs, FF01: three legs, RF13: six legs, FF02: four legs). One flight leg (FF01 leg 1) was flown along a slightly shifted flight track, compared to the Mt-A-2b transect (thin red line in Fig. 1), and is only included in the analysis where specifically stated.

The topography of the SI is rough and structured with a sequence of valleys oriented parallel to the mountain range. Along the Mt-A-2b transect, several individual peaks can be identified. These peaks are labeled in Fig. 3a, and their respective names, latitudes, and

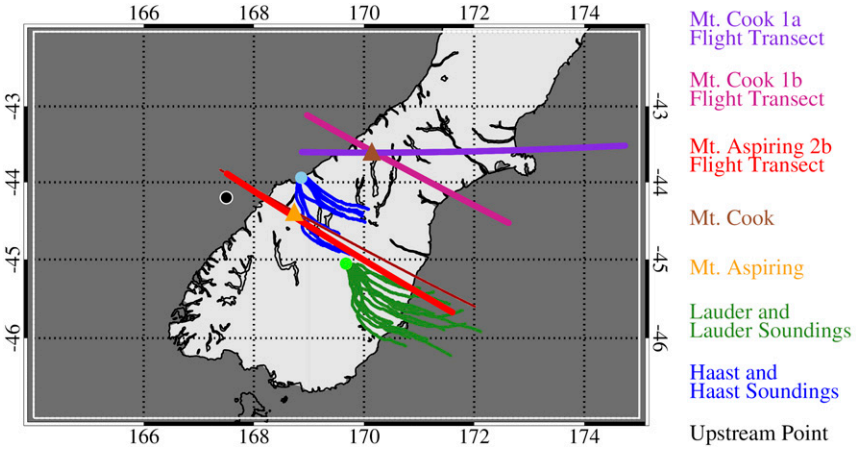

FIG. 1. Map of the SI of NZ with colored flight transects Mt. Cook 1a and 1b (hereinafter Mt-C-1a and Mt-C-1b, respectively), Mt-A-2b, the radiosonde stations Haast and Lauder, and the radiosonde flight tracks during the IOP 9. The thin red line close to the Mt-A-2b flight transect marks FF01 leg 1. In addition, the upstream point (44.2°S, 167.5°E) used in the ECMWF analyses is shown. Triangles denote the location of Mt. Aspiring and Mt. Cook in the respective color coding.

longitudes are listed in Table 1. Their positions on the map can be found in Fig. 3b. Mt. Aspiring is the highest peak along this track. The outstanding peak at 20-km distance belongs to the Dunstan Mountains in central Otago, located directly upstream of the radiosonde and Rayleigh lidar station in Lauder (Fig. 1). All GV flight legs were flown within the stratosphere at around 12- and 14-km altitude, whereas the Falcon crossed the tropopause during both FF01 and FF02 (Table 2, Fig. 2).

For this study, the 1-Hz in situ flight-level data of the GV and Falcon were used. For the GV, general measurement uncertainties are given in Smith et al. (2016). For the Falcon, measurement uncertainties can be found in Rotering (2011) and Giez et al. (2017). Only GPS height data (no differential GPS) are available for the Falcon during the DEEPWAVE campaign. On board the GV, upper-atmosphere observations were performed using an Advanced Mesospheric Temperature Mapper (AMTM) imaging system. This instrument measures the intensity

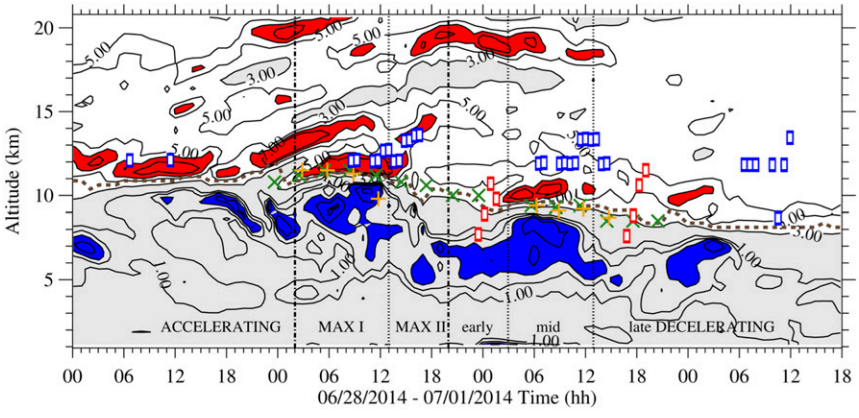

FIG. 2. ECMWF IFS Brunt–Väisälä frequency N^2 with colored contours of $\geq 6 \times 10^{-4}\,s^{-2}$ in red and $\leq 0.5 \times 10^{-4}\,s^{-2}$ in blue. Gray shaded are areas of $N^2 \leq 3 \times 10^{-4}\,s^{-2}$. The brown dashed line, the orange solid line, and the green diagonal crosses give the thermal tropopause calculated from IFS data, as well as from Haast and Lauder soundings, respectively. Blue and red rectangles show altitudes of all GV and Falcon mountain legs. Dotted–dashed vertical lines are the separation into accelerating, maximum, and decelerating forcing phases. Dotted vertical lines further show the division into maximum forcing phase I and II and early, mid-, and late decelerating forcing phases.

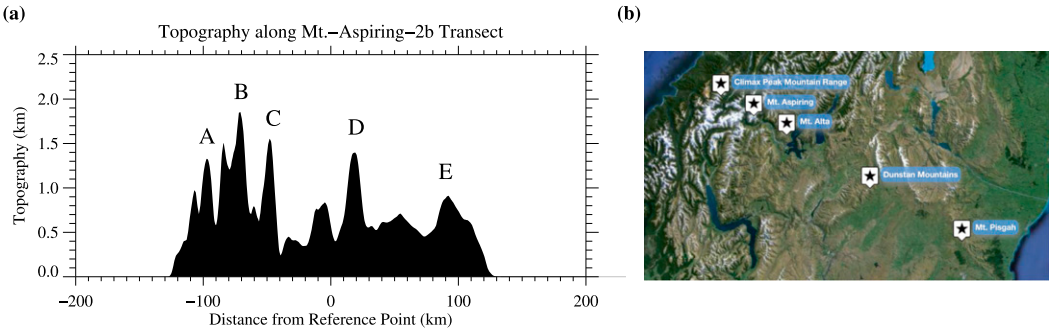

FIG. 3. (a) WRF topography with the finest obtainable resolution of 30 arc s along the Mt-A-2b transect with labeled peaks. For the projection upon the flight tracks, the Lambert projection is used, with a 1-km grid spacing and the topography data bilinearly interpolated to the flight track coordinates. The middle of the island along the transect is taken as the reference point (distance = 0 km). (b) Map over the SI of NZ with the identified mountains along the Mt-A-2b transect (via Google Earth view 2015).

and rotational temperature of the bright OH airglow layer located at ≈87-km altitude. OH is a vibrationally excited molecule of oxygen (O) and hydrogen (H). It is produced by the chemical reactions of either $H + O_3$ or $O + HO_2$ (see Snively et al. 2010). In statistical thermodynamics, the rotational temperature is the temperature at which the thermal population of the rotational states is such as to give rise to the observed rotational spectrum, in terms of the relative intensities of the different transitions. The equivalence of the OH rotational temperature and the temperature of the emitting atmosphere, established by Wallace (1962), allows us to measure the mesopause temperature at the altitude of the OH airglow layer. Therefore, this emission has been extensively used to study waves propagating through the mesosphere–lower thermosphere (MLT) region (e.g., Pautet et al. 2014; Bossert et al. 2015; Pautet et al. 2016; Eckermann et al. 2016).

Altogether, 23 radiosondes were launched from Haast on the upstream side of the Southern Alps and from Lauder in the lee of the main ridge of the Southern Alps. The locations of radiosonde stations and the balloon trajectories are given in Fig. 1. These soundings (eight from Haast and 15 from Lauder) complemented the airborne measurements with respect to vertical observations from the ground up to the stratosphere. A maximum altitude of 36 km was achieved, and the average flight duration was 2.5 h.

In addition, DLR operated a mobile middle atmosphere Rayleigh lidar at Lauder. On the basis of integrated range-corrected photon count profiles (which are proportional to atmospheric density profiles), temperatures are retrieved assuming hydrostatic equilibrium. Temperature profiles are available from the middle stratosphere up to the mesosphere from ~30- to 80-km altitude. Details of the instrumentation of the lidar can be found in Kaifler et al. (2015). Measurement uncertainties, as well as the calculation of the temperature perturbations T' applying a Butterworth filter, are described in Ehard et al. (2015). During IOP 9, the lidar operated exclusively during the entire night of 30 June 2014. The determination of the averaged gravity wave potential energy density (GWPED) in the upper stratosphere (28–44 km), stratopause (44–60 km), and mesosphere (60–76 km) as a measure of the gravity wave activity in the three altitude ranges is explained in Kaifler et al. (2015). Here, a 1-h running mean of the 2-min vertically averaged observational data is calculated.

Six-hourly operational analyses valid at 0000, 0600, 1200, and 1800 UTC and 1-hourly high-resolution forecasts at intermediate lead times (+1, +2, +3, +4, +5, +7, +8, +9, +10, and +11 h) of the 0000 and 1200 UTC forecast runs of the Integrated Forecast System (IFS) of the European Centre for Medium-Range Weather Forecasts (ECMWF) are further used to visualize the temporal evolution of the upstream conditions at 44.20°S, 167.50°E (Fig. 1). The IFS cycle 40r1 has a horizontal resolution of about 16 km, 137 vertical model levels, and a model top at 0.01 hPa, with numerical damping starting at 10 hPa (Jablonowski and Williamson 2011).

TABLE 1. Identified mountains along the Mt-A-2b transect from west to east with their respective latitudes and longitudes. The letters and distances refer to the marked peaks in Fig. 3a and their respective distance to the reference point (middle of the island along the cross section).

	Distance (km)	Name	Lat	Lon
A	≈−95	Part of the Climax Peak	44.33°S	168.47°E
B	≈−70	Mount Aspiring	44.45°S	168.74°E
C	≈−45	Mount Alta	44.57°S	169.00°E
D	≈20	Dunstan Mountains	44.87°S	169.69°E
E	≈90	Part of Mount Pisgah	45.18°S	170.44°E

TABLE 2. Serial leg numbers as counted in Fig. 2, research flight (RF: GV; FF: Falcon), flight leg number, respective forcing phase [accelerating (acc), maximum (max), decelerating (dec)], day, mean leg time, leg-averaged flight altitude, flight transect (Mt. Aspiring, Mt. Cook), and status of cross-mountain legs during DEEPWAVE IOP 9. A checkmark in the status column is provided for Mt-A-2b flight legs that were analyzed in more detail in this paper.

Serial No.	Flight	Leg No.	Forcing phase	Day	Mean time (UTC)	Mean altitude (km)	Transect	Status
1	RF11	1	Acc	28 Jun	0637	12.1	Mt-C-1b	
2	RF11	8	Acc	28 Jun	1123	12.1	Mt-C-1b	
3	RF12	1	Max I	29 Jun	0838	12.1	Mt-A-2b	✓
4	RF12	3	Max I	29 Jun	0915	12.1	Mt-C-1b	
5	RF12	6	Max I	29 Jun	1108	12.0	Mt-A-2b	
6	RF12	8	Max I	29 Jun	1145	12.1	Mt-C-1b	
7	RF12	10	Max I	29 Jun	1223	12.7	Mt-A-2b	✓
8	RF12	12	Max I	29 Jun	1259	12.7	Mt-C-1b	
9	RF12	14	Max II	29 Jun	1336	12.1	Mt-A-2b	✓
10	RF12	16	Max II	29 Jun	1413	12.1	Mt-C-1b	
11	RF12	18	Max II	29 Jun	1451	13.3	Mt-A-2b	✓
12	RF12	20	Max II	29 Jun	1526	13.3	Mt-C-1b	
13	RF12	22	Max II	29 Jun	1603	13.6	Mt-A-2b	✓
14	RF12	24	Max II	29 Jun	1626	13.6	Mt-C-1b	
15	FF01	1	Early dec	29 Jun	2330	7.7	Mt-A-2b different	
16	FF01	2	Early dec	30 Jun	0014	8.9	Mt-A-2b	✓
17	FF01	3	Early dec	30 Jun	0057	10.7	Mt-A-2b	✓
18	FF01	4	Early dec	30 Jun	0137	9.7	Mt-A-2b	✓
19	RF13	1	Mid-dec	30 Jun	0635	11.9	Mt-A-2b	✓
20	RF13	3	Mid-dec	30 Jun	0711	11.9	Mt-C-1b	
21	RF13	6	Mid-dec	30 Jun	0903	11.9	Mt-A-2b	✓
22	RF13	8	Mid-dec	30 Jun	0939	11.9	Mt-C-1b	
23	RF13	10	Mid-dec	30 Jun	1016	11.9	Mt-A-2b	✓
24	RF13	12	Mid-dec	30 Jun	1053	11.9	Mt-C-1b	
25	RF13	13	Mid-dec	30 Jun	1130	13.3	Mt-A-2b	✓
26	RF13	15	Mid-dec	30 Jun	1206	13.4	Mt-C-1b	
27	RF13	17	Mid-dec	30 Jun	1243	13.3	Mt-A-2b	✓
28	RF13	19	Late dec	30 Jun	1319	13.4	Mt-C-1b	
29	RF13	21	Late dec	30 Jun	1357	11.9	Mt-A-2b	✓
30	RF13	23	Late dec	30 Jun	1434	11.9	Mt-C-1b	
31	FF02	1	Late dec	30 Jun	1654	7.6	Mt-A-2b	✓
32	FF02	2	Late dec	30 Jun	1741	8.8	Mt-A-2b	✓
33	FF02	3	Late dec	30 Jun	1822	10.6	Mt-A-2b	✓
34	FF02	4	Late dec	30 Jun	1909	11.5	Mt-A-2b	✓
35	RF14	1	Late dec	1 Jul	0643	11.8	Mt-C-1a	
36	RF14	2	Late dec	1 Jul	0722	11.8	Mt-C-1a	
37	RF14	3	Late dec	1 Jul	0802	11.8	Mt-C-1a	
38	RF14	6	Late dec	1 Jul	1000	11.8	Mt-C-1a	
39	RF14	7	Late dec	1 Jul	1040	8.7	Mt-C-1a	
40	RF14	8	Late dec	1 Jul	1123	11.8	Mt-C-1a	
41	RF14	9	Late dec	1 Jul	1204	13.4	Mt-C-1a	

Moreover, mesoscale numerical simulations with the Weather Research and Forecasting (WRF;[1] Skamarock et al. 2008; Skamarock and Klemp 2008) Model are performed. With the use of Advanced Research WRF version 3.7, atmospheric simulations are generated processing operational ECMWF analyses as initial and boundary conditions. Two nested model domains are centered at 43°S, 169°E over the SI of NZ. The inner domain has a horizontal resolution of 2 km with 553 × 505 grid points in the *x*–*y* plane, and the outer domain has a resolution of 6 km with 440 × 430 grid points. There are 138 terrain-following levels used in the vertical, with level distances stretching from 85 m near the surface to about 170 m at 1-km altitude. Level distances

[1] Freely available: www2.mmm.ucar.edu/wrf/users/download/get_source.html

are kept nearly constant at 170 m in the troposphere. Above 10-km altitude, they are further stretched from 170 m to 1.5 km at the model top, which is set at 2 hPa (about 40 km). Implicit damping of the vertical velocity (Rayleigh damping layer; Klemp et al. 2008) is applied to the uppermost 7 km of the model domain. This damping layer impedes wave reflection at the model top. The flow structure up to 25-km altitude is only marginally influenced when using damping layers of 10- and 15-km thickness (not shown). The WRF simulations are initialized at 1800 UTC 28 June 2014 with IFS operational analyses and are run for 54 h until 0000 UTC 1 July 2014. The usefulness of the combination and comparison of the high-resolution output of the WRF simulations with lidar, aircraft, and radiosonde data was already demonstrated by Ehard et al. (2016) and Wagner et al. (2017).

To investigate the flow development along the Mt-A-2b cross section under quasi-steady background conditions, six simulations are performed with the WRF Model in a two-dimensional idealized setup covering the core period of the transient event. The model domain has a horizontal extent of 400 km and a model top at 40 km. The same vertical levels as in the real case simulations are used, and the lower boundary is defined by the topography along the Mt-A-2b cross section. These runs are initialized with vertical profiles of horizontal wind and potential temperature taken at the first upstream point of the Mt-A-2b cross section from the innermost domain of the transient simulation. The six upstream profiles are taken every 6 h between 0000 UTC 29 June and 0600 UTC 30 June and are kept constant throughout each simulation, covering 48 h. In the 2D WRF Model, open boundary conditions are used in flow direction. Note that horizontal winds are projected to a wind direction of 300° (u_{track}), which is the direction of the Mt-A-2b transect (Fig. 1). All idealized simulations are run without moisture and radiation effects.

From both the WRF and the in situ flight-level data, vertical energy and momentum fluxes are calculated according to the method of Smith et al. (2008), with a leg integration of $p'w'$ (EF_z), $u'w'$ (MF_x), $v'w'$ (MF_y), and $u'_{\text{track}}w'$ (MF_{track}) in units of W m^{-1} and N m^{-1}, respectively. The perturbation quantities of wind (u', v', w') and pressure (p') are calculated by detrending the data of each leg and removing the mean over the leg. The detrending is performed by subtracting a linear least squares fit. Before detrending, the pressure is corrected for altitude changes (Smith et al. 2008). The detrending of p corresponds to a geostrophic correction (Smith et al. 2016). Detrending of the wind variables is especially necessary for legs where synoptic-scale systems may cause gradients. For the in situ flight-level data, a wavelet analysis is further performed to quantify gravity wave propagation both spatially and spectrally. In extension to the approach of Woods and Smith (2010, 2011), the energy and momentum flux cospectra are reconstructed in such a way that the integrated cospectra directly result in the leg-integrated flux values obeying the correct units. This extended wavelet transform and the calculation of significant parts of the cospectra are described in more detail in the appendix.

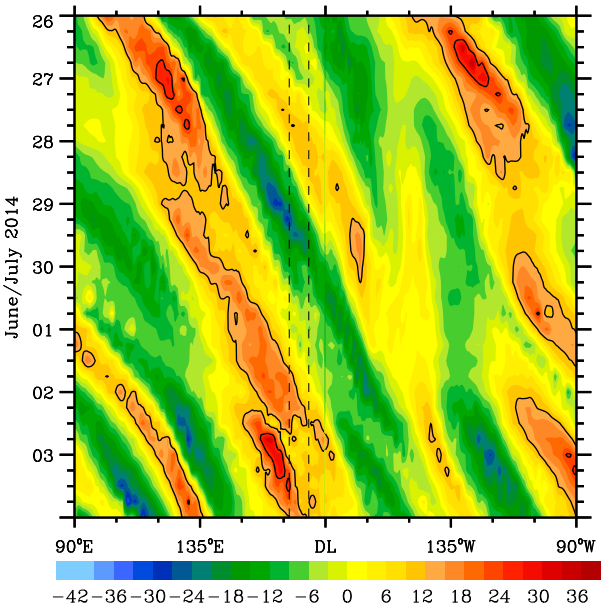

FIG. 4. Hovmoeller diagram of the meridional wind component (m s^{-1}) at 700 hPa obtained from the ECMWF IFS. Data were spatially averaged between 40° and 45°S. The dashed lines mark the location of the SI. Black contour lines are shown for 12, 24, and 48 m s^{-1}. DL in the longitude axis marks the date line.

3. Meteorological evolution during IOP 9

The tropospheric flow during IOP 9 started as a so-called trough–northwest regime characterized by a low-level northwesterly flow (28–30 June 2014) and proceeded to a trough regime with more westerly low-level flow on 1 July 2014 (Table 1 and Fig. 2f in Gisinger et al. 2017). Figure 4 illustrates the eastward propagation of a Rossby wave train by means of the 700-hPa meridional wind component v averaged between 40° and 45°S. During the period from 28 to 29 June 2014, v swapped sign from positive to negative over the SI. This indicates the passing ridge axis prior to the trough in the west. This transition caused increasing northwesterly and westerly winds, associated with a passing occluding frontal system (Figs. 5a,b). At 1200 UTC 29 June, a broad band of horizontal winds $V_H > 20\ \text{m s}^{-1}$ was

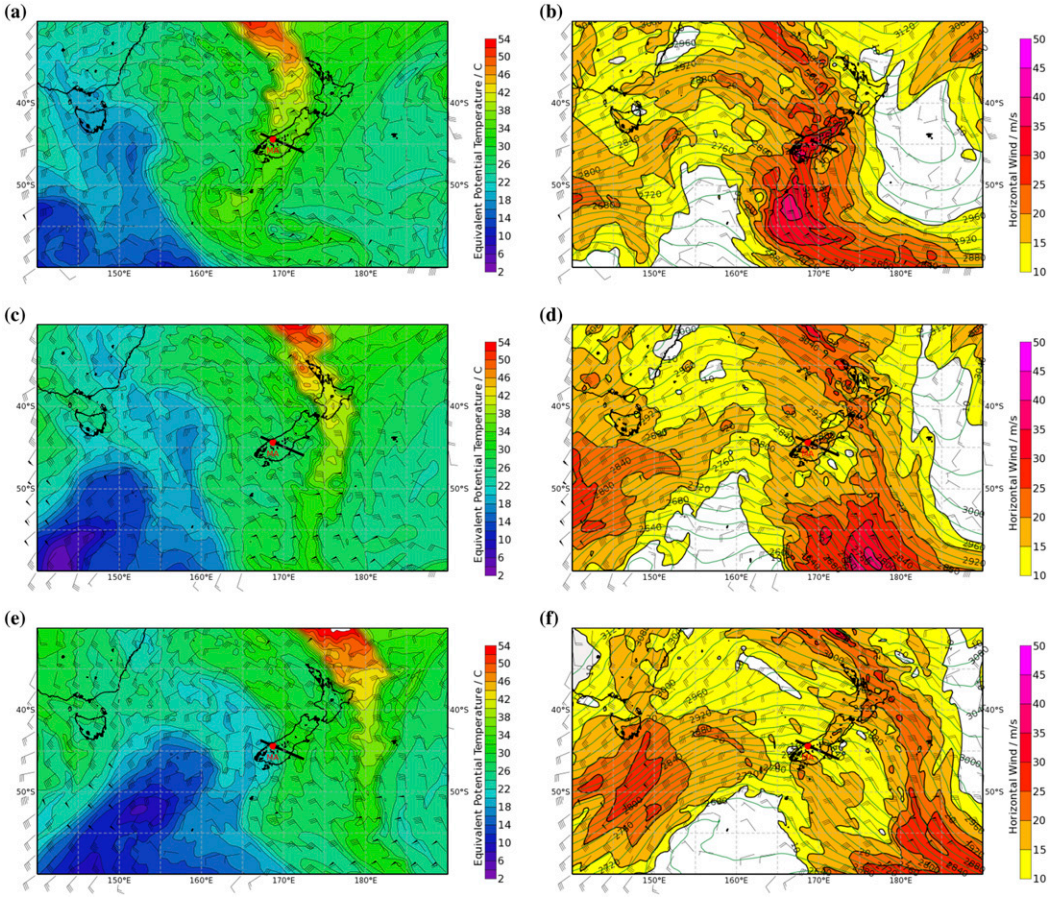

FIG. 5. (a),(c),(e) ECMWF IFS equivalent potential temperature and (b),(d),(f) horizontal wind with wind barbs and 20-m-spaced contours of geopotential height at 700 hPa at 1200 UTC 29 Jun, 0000 UTC 30 Jun, and 1200 UTC 30 Jun 2014. The transect Mt-A-2b is superimposed as a black line in the individual panels. The location of Mt. Aspiring is marked with a red dot.

directed almost perpendicular to the mountain range of the SI (Fig. 5b). In the following 24 h, the wind direction stayed nearly constant at 700 hPa, but V_H decreased in magnitude, as displayed in Figs. 5d and 5f. The cold front associated with the slowly eastward-migrating trough reached the SI at 700 hPa at 1200 UTC 30 June (Fig. 5e). According to Fig. 4, the northerly component of the tropospheric flow lasted until 1 July 2014. Afterward, the meridional wind component v became positive again, indicating the passage of the trough axis and the transition to southwesterly winds.

In Fig. 6, the time series of the IFS upstream cross-mountain wind component ($U_\perp$, direction ≈322°), averaged over the lowest 4 km of the troposphere, is shown together with radiosonde observations from Haast and Lauder for the 4-day period of IOP 9. The cross-mountain wind direction matches the mean wind direction at low levels below crest height and is therefore also approximately the wave vector direction. The cross-mountain winds increased from about 2 to 22 m s^{-1} from 0000 UTC 28 June to 1000 UTC 29 June 2014 and decreased almost to the initial value thereafter (Fig. 6). The radiosonde cross-mountain winds generally follow the course of the IFS time series. However, larger deviations occurred on 30 June 2014. These deviations can be explained by the cold front approaching from the west (Fig. 5e) and passing first the upstream point, then Haast, and last Lauder, causing winds to decrease at Haast and Lauder later in time.

From Fig. 6, it is found that IOP 9 is centered on a strong forcing period of $U_\perp > 15$ m s^{-1} between 0200 and 2000 UTC 29 June 2014 (maximum forcing phase). Before and after, weak to moderate cross-mountain winds ranging up to 5 and 15 m s^{-1}, respectively, define the accelerating and decelerating forcing phases of this transient event. The evolution of the cross-mountain wind $U_\perp$ can be approximated by $U_\perp(t) = U_{\perp 0} + \Delta U_\perp \cos^2(\pi t/t_{\text{tot}})$, which is shown as a dashed line in Fig. 6. Here, $U_{\perp 0} = 5$ m s^{-1} is the

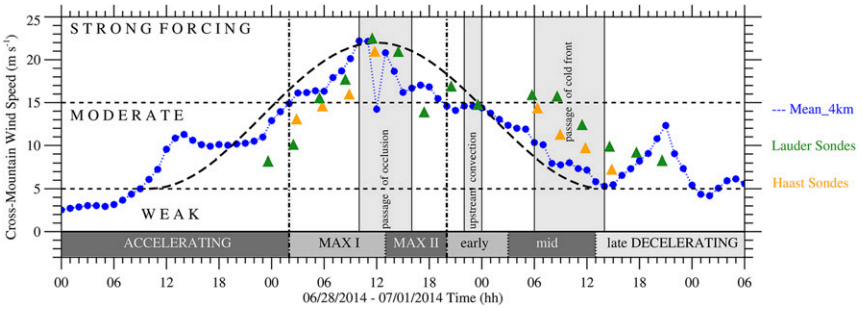

FIG. 6. ECMWF IFS upstream cross-mountain wind speed (at 44.2°S, 167.5°E) during IOP 9 from 0000 UTC 28 Jun to 0600 UTC 1 Jul 2014. Mean upstream values were calculated as averages over the lowest 4 km (blue). Green and orange triangles depict the respective values for the Lauder and Haast sondes. Up to 5 m s^{-1} wind speed, the forcing is referred to as "weak," from 5 to 15 m s^{-1} is "moderate," and more than 15 m s^{-1} is "strong." The dotted–dashed vertical lines refer to the division into accelerating, maximum, and decelerating forcing. Also, periods of synoptic events like passing fronts and convection are marked. The dashed black curve marks an approximation of the transient forcing following $U_\perp(t) = U_{\perp 0} + \Delta U_\perp \cos^2(\pi t/t_{\text{tot}})$, with $U_{\perp 0} = 5$ m s^{-1}, $\Delta U_\perp = 17$ m s^{-1}, and $t_{\text{tot}} = 53$ h.

value at the beginning and at the end of the transient event, $\Delta U_\perp = 17\,\text{m s}^{-1}$ is the amplitude, and $t_{\text{tot}} = 53$ h is the period of the synoptic-scale low-level forcing.

According to the findings of Gisinger et al. (2017), the peculiarity of IOP 9 was the southward deflection of the core of the subtropical jet stream (STJ) to about 40°S in the region of NZ (also see Fig. 7b). The southward deflection of the subtropical jet is evident at 200 hPa, especially at early times (Fig. 7b). Later, the 200-hPa winds decreased markedly over the SI (Figs. 7d,f). At lower levels, a branch of the STJ separated from the main jet and diverted south (Fig. 7a). This branch of the STJ passed the SI during the displayed sequence (Figs. 7a,c). At 1200 UTC 30 June 2014, 300-hPa winds increased again, with the approaching front reaching about 35 m s^{-1} over the SI (Fig. 7e). This changing upper-tropospheric wind conditions resulted in varying propagation conditions in the UTLS region for the excited mountain waves during IOP 9.

Figure 8a displays vertically smoothed and temporally averaged profiles of $U_\perp$ from the IFS taken at the above-defined upstream point in Fig. 1. A double-jet structure dominated the wind profile in the UTLS during the first half of 29 June 2014 (blue solid line in Fig. 8a). The respective $U_\perp$ maxima of 40 m s^{-1} at ≈11 km and of 32 m s^{-1} at ≈15-km altitude belong to the split branch of the STJ and the STJ itself (Figs. 7a,b). In between the double jet at around 13.5-km altitude, the minimum wind speed of $U_\perp$ was 25 m s^{-1}. As the STJ passed the SI, the upper peak of the double jet reduced to 25 m s^{-1} (violet line of 1400–1600 UTC average in Fig. 8a). The lower-level peak broadened in altitude and became smaller in magnitude. The depth of minimum wind layer between the two jets narrowed, and the $U_\perp$ decreased in this layer, creating a shallow layer of strong negative shear between 12- and 13.5-km altitude (shaded in Fig. 8a).

At the end of 29 June 2014, the lower-level split-branch jet had moved downstream the SI (Fig. 7c), and only a weak wind maximum remained at ≈10-km altitude (green line in Fig. 8a). At this time, the edge of the STJ was located over the SI (Fig. 7d), with maximum upstream $U_\perp$ of ≈30 m s^{-1} at 14-km altitude (green line in Fig. 8a). Above, a still-sharp wind reduction to 18 m s^{-1} within an altitude range of 1.5 km is found. Later, after the passage of the cold front (Fig. 5e), the wind profile became more uniform near the tropopause (Fig. 8a). The difference between the wind speed in the lower and middle stratosphere decreased from 20 m s^{-1} on 29 June to 10 m s^{-1} later on 30 June (Fig. 8a). At all times, the cross-mountain wind speeds increased above 30-km altitude due to the presence of the polar night jet (PNJ) over the SI.

At the time of occurrence of the double-jet structure, a low-stability layer with reduced values of the squared Brunt–Väisälä frequency $N^2 = g\partial \ln(\theta)/\partial z$ was located beneath the tropopause (cf. blue shaded values of $N^2 < 0.5 \times 10^{-4}\,\text{s}^{-2}$ in Fig. 2). This resulted in a sharp tropopause and a pronounced tropopause inversion layer (TIL; Birner et al. 2002), which was frequently found over NZ during DEEPWAVE (Fig. 4a in Gisinger et al. 2017). As visible in Fig. 2, the tropopause descended from about 11.5- to about 8.5-km altitude from 0800 UTC 29 June to 1900 UTC 30 June. Consequently, the Scorer parameter (Scorer 1949),

$$\ell(z) = \sqrt{\frac{N^2(z)}{U_\perp^2(z)} - \frac{1}{U_\perp(z)}\frac{d^2U_\perp(z)}{dz^2}}, \qquad (1)$$

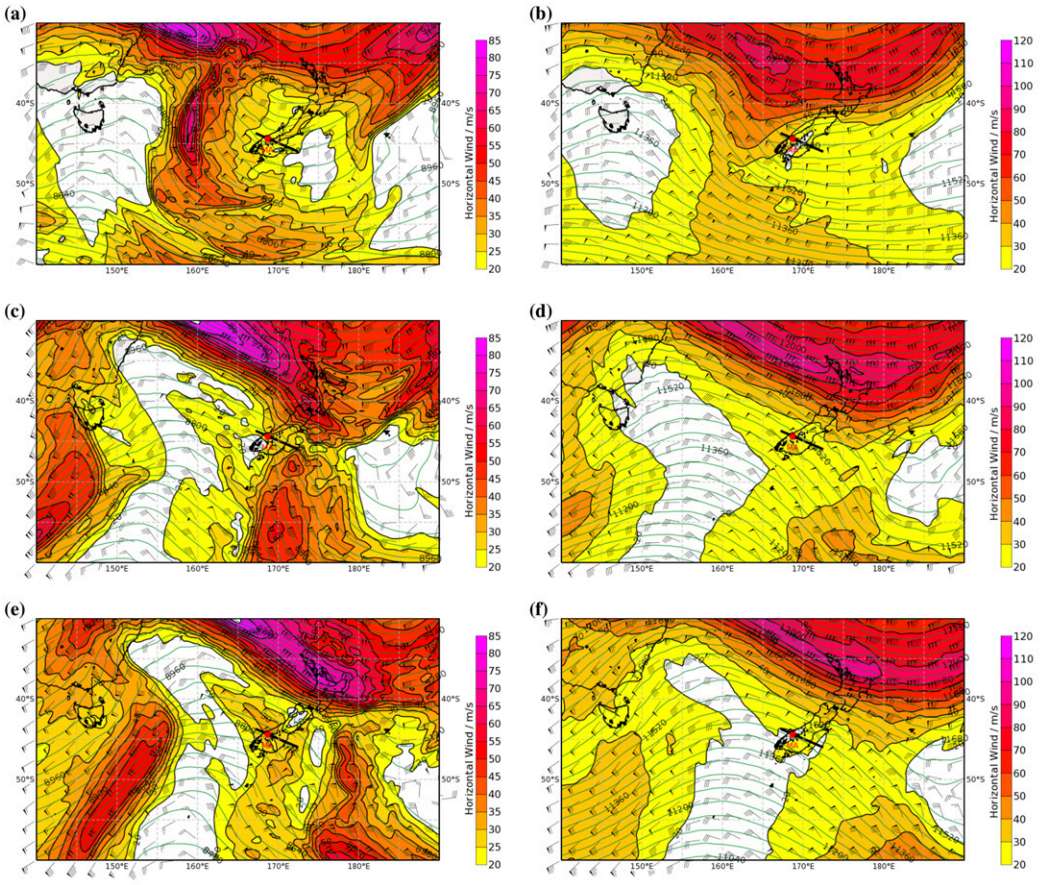

FIG. 7. ECMWF IFS horizontal wind speed with wind barbs and 40-m-spaced contours of geopotential height at (a) 300 and (b) 200 hPa at 0000 UTC 29 Jun, (c) 300 and (d) 200 hPa at 0000 UTC 30 Jun, and (e) 300 and (f) 200 hPa at 1200 UTC 30 Jun 2014.

shows a distinct minimum varying between 8.5- and 6-km altitude (Fig. 8b). In linear, steady-state theory, the Scorer parameter indicates vertically propagating waves for horizontal wavenumbers $k = 2\pi/\lambda_x < \ell$ and evanescent waves for $k > \ell$. The critical wavenumber $k_{\text{crit}} = \ell$ and the corresponding critical horizontal wavelength $\lambda_{\text{crit}} = 2\pi/\ell$ mark the transition between both regimes. The pronounced low-stability layer below the tropopause resulted in a large $\lambda_{\text{crit}} \approx 30$ km during early 29 June (blue line of 0800–1000 UTC average in Fig. 8b). Until late 30 June 2014, increasing stabilization (Fig. 2) and decreasing wind speeds lead to a smaller $\lambda_{\text{crit}} \approx 10$ km in the upper troposphere (orange line in Fig. 8b).

The analysis of the meteorological situation around the SI revealed the low-level forcing and the propagation conditions in the UTLS region. Both will have an influence on the observed wave activity at flight level.

Finally, Fig. 9 illustrates the mesoscale flow by means of the vertical wind component and isentropic surfaces from the innermost domain of the WRF simulations interpolated along the Mt-A-2b transect. Four different times are selected to cover the maximum and decelerating forcing phases. At all times, up- and downdrafts, apparently associated with individual mountain peaks, dominate the vertical wind field in the troposphere. The tropopause, marked by decreasing spacing of the isentropes, descended during the displayed period, and the TIL weakened (cf. Figs. 9a,d). In the lower stratosphere, propagating waves of varying intensity and vertical extent appear mainly over the mountain peaks and are characterized by vertical wavelengths of 5–6 km. During the decelerating forcing phase (Figs. 9c, d) and with the weakening of the TIL (Fig. 2), the amplitudes of the simulated gravity waves in the stratosphere become larger with more than 3 m s^{-1} (Fig. 9d). Most pronounced in Fig. 9c, isentropes become very steep in the altitude region between ≈15 and ≈20 km. Near the end of IOP 9, gravity waves of even larger amplitudes, having horizontal wavelengths of about 20 km, and large vertical wavelengths are found at the lower edge of the PNJ (Fig. 9d, orange profile above 30 km in Fig. 8a).

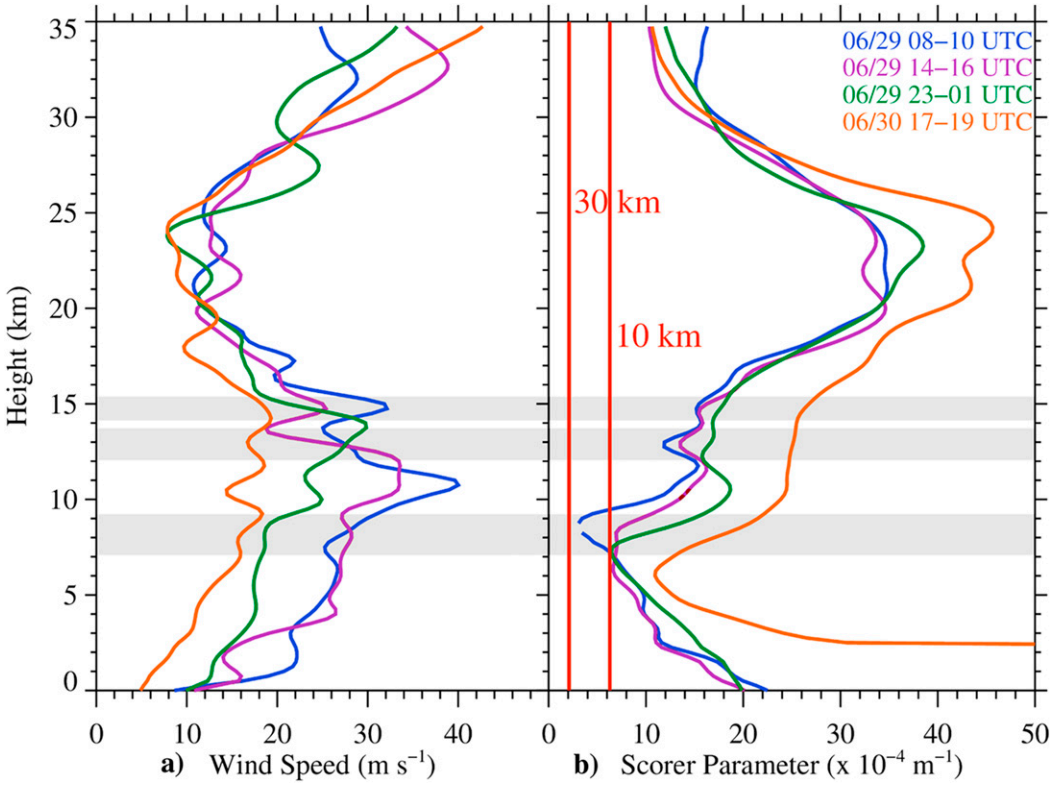

FIG. 8. ECMWF IFS upstream (a) cross-mountain wind speed and (b) Scorer parameter smoothed over 750 m in the vertical during 3-h windows of maximum forcing phase part I (0800–1000 UTC 29 Jun), part II (1400–1600 UTC 29 Jun), early (2300–0100 UTC 29 Jun), and late (1700–1900 UTC 30 Jun) decelerating forcing phases. In red, the critical wavenumbers and wavelengths for propagation based on an argument from steady-state theory are given for different periods in (b). Waves are able to propagate as long as the ambient Scorer parameter is larger than the selected wavenumber. From bottom to top, the altitude range of inhibited propagation for waves shorter than 50-km horizontal wavelength during maximum forcing phase part I (0800–1000 UTC 29 Jun), of strong negative shear during maximum forcing phase part II (1400–1600 UTC 29 Jun), and during early decelerating forcing phase (2300–0100 UTC 29 Jun) are shaded in gray.

4. Results

Aircraft observations along the Mt-A-2b transect exist only during maximum (covered by RF12) and decelerating (covered by FF01, RF13, and FF02) forcing phases. These different phases are further divided into maximum forcing phases part I and II and in early, mid-, and late decelerating forcing phases, according to the changing propagation conditions in the UTLS (see Fig. 2, Table 2). In this section, we analyze the wave response in the UTLS (section 4a) by means of vertical displacements and along-track momentum fluxes. The vertical propagation into the mesosphere is investigated in section 4b.

a. Wave response in the UTLS

1) VERTICAL DISPLACEMENTS

Figure 10 illustrates the varying wave activity over the Mt-A-2b transect by means of vertical displacement $\eta = \int_0^x [w'(x)/u_{\text{track}}(x)]\, dx_{\text{track}}$ (Smith et al. 2008), derived from the flight-level vertical velocity perturbation w' and the along-track wind component u_{track} of the four research flights RF12, FF01, RF13, and FF02.

During the maximum forcing phase, η decreases slightly from the upstream locations to the middle of the main mountain ridge, where a pronounced increase of about 1300 m is found [RF12; Fig. 10a; see also Fig. 9a in Smith et al. (2016)]. Small-amplitude fluctuations of η extend downwind over the SI. Especially for leg 1 and leg 18, those fluctuations show small horizontal scales of $\lambda_x \approx 10$ km downstream of the Dunstan Mountains, which is located at 20-km distance. Legs 18 and 22 further show a region of very small-scale perturbations ($\lambda_x < 2$ km) between −100- and −75-km distance over the Mt. Aspiring massif. In Smith et al. (2016), the threshold of $\lambda_x = 2$ km is used to denote turbulent motions. We follow this terminology in this study.

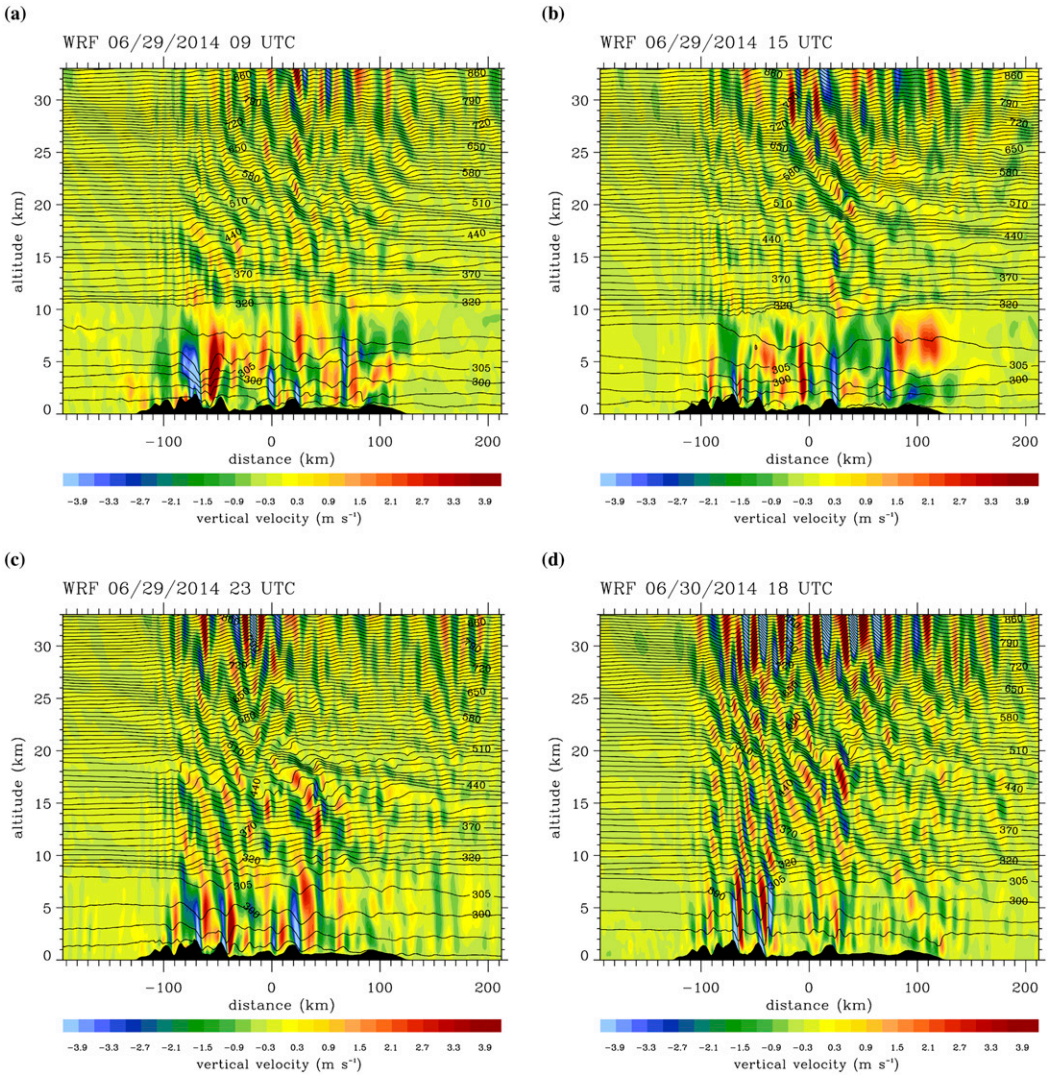

FIG. 9. WRF vertical wind along the Mt-A-2b transect up to 33-km altitude (sponge layer is excluded) with 5-K-spaced isentropes up to 320 K and 10-K-spaced isentropes above at (a) 0900, (b) 1500, and (c) 2300 UTC 29 Jun and (d) 1800 UTC 30 Jun.

The beginning of the decelerating forcing phase was covered by the subsequent Falcon research flight FF01 (Fig. 10b). It reveals vertical displacements with peak-to-peak amplitudes up to 1500 m extending over the main mountain ridge (around distance = −80 km). This part of the η curves is dominated by long waves with $\lambda_x \approx$ 200 km. Their upstream phase tilt with height (estimated phase line in black in Fig. 10b) is characteristic for upward-propagating hydrostatic mountain waves based on steady-state assumptions. Supporting this finding, the mountain waves in the WRF simulations also show an upstream phase tilt in the w field at about the same horizontal distance ($\approx$ −60 km) between 8- and 11-km altitude (Fig. 9c). In addition, shorter ($\lambda_x \approx$ 20–30 km), high-amplitude (up to 1200 m) η oscillations are found above and in the lee of the Dunstan Mountains (at 20-km distance) and above the range of Mt. Pisgah (at 90-km distance; Fig. 10b). As mentioned above, FF01 leg 1 had slightly different track coordinates than the other legs, especially at the downstream part of the leg (thin red line in Fig. 1). Therefore, the oscillations observed directly over the Dunstan Mountains could not be detected during FF01 leg 1. In agreement with the other legs, the large-scale response with $\lambda_x \approx$ 200 km is well captured. Compared to RF12, small-scale wave activity with $\lambda_x \approx$ 10 km is only found downstream of the SI (leg 3 and leg 4).

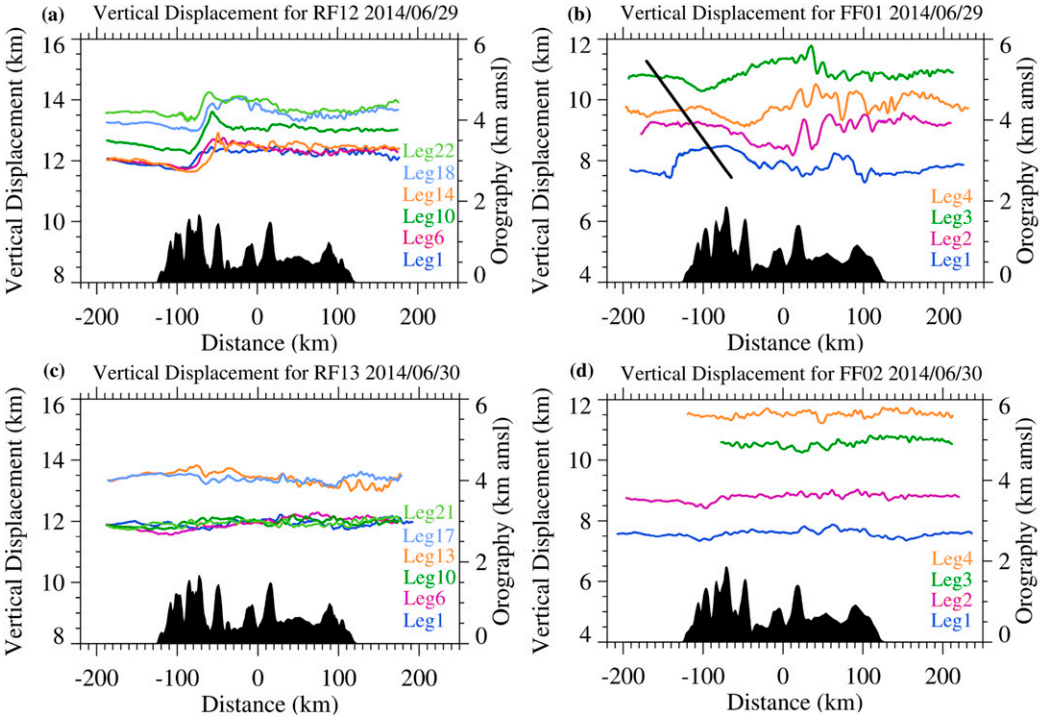

FIG. 10. Vertical displacement for the flight legs of (a) RF12 and (b) FF01 on 29 Jun 2014 and (c) RF13 and (d) FF02 on 30 Jun 2014 with underlying topography along the Mt-A-2b transect. For the Falcon legs, the topography originates from the WRF Model with the finest obtainable resolution of 30 arc s. For the GV flight tracks, the topographic height was provided by the NCAR Earth Observing Laboratory (EOL). In (b), an estimated phase line (black) of the long waves ($\lambda_x \approx 200$ km) is shown to guide the eye.

During the mid- and late decelerating forcing phases, the observed wave activity is strongly reduced. While peak-to-peak η amplitudes of up to 1500 m are found during RF12 and FF01, they are reduced during RF13 and FF02, reaching maximum values of around 500 m (Figs. 10c,d). The large-scale waves that showed up in the vertical displacements of FF01 can no longer be clearly found for RF13 and FF02 (Figs. 10c,d). In addition, the small-scale η oscillations do not show a strong connection to underlying dominant topographic features toward the end of IOP 9 (Fig. 10d). The interim occurrence of horizontally long waves and the pronounced temporal decay of the η amplitudes in the decelerating forcing phase are the key findings of the vertical displacement analyses.

2) MOMENTUM FLUXES

The transience of the wave response during IOP 9 is further quantified by means of vertical fluxes of along-track momentum MF_{track}. Figure 11a displays all leg-integrated aircraft observations and the respective fluxes calculated from the transient WRF simulation at typical flight altitudes of 8 km (upper troposphere) and 13 km (lower stratosphere). $MF_{track} < 0$ mainly indicates downward transport of positive momentum, that is, upward-propagating gravity waves in the westerly flow. A change of sign denotes a change of vertical propagation direction. In Fig. 11, we show $-MF_{track}$ and use the values without sign in the following, but we point out sign reversals when present.

The observed MF_{track} increases from $\approx$10 to $\approx$70 kN m^{-1} in the maximum forcing phase (green dots of RF12 in Fig. 11a). During the early decelerating forcing phase, the leg-integrated fluxes spread by $\approx$120 kN m^{-1} between the tropospheric (first violet dot at 130 kN m^{-1} in Fig. 11a) and the stratospheric (last two violet dots at $\approx$10 kN m^{-1} in Fig. 11a) flight altitudes of FF01. In the subsequent mid-decelerating forcing phase, RF13 shows stratospheric flux values between $\approx$15 and $\approx$30 kN m^{-1}. During the final research flight FF02, $-MF_{track}$ is $<$15 kN m^{-1} and even reverses sign.

The simulated tropospheric $-MF_{track}$ (black dashed line in Fig. 11a) oscillates throughout the IOP 9. Maximum values of about 200 kN m^{-1} are attained during the early decelerating forcing phase. The simulated stratospheric $-MF_{track}$ (light blue dashed line in Fig. 11a) is about constant at $\approx$40 kN m^{-1} during maximum forcing phase part I. The maximum of $\approx$130 kN m^{-1} occurs at

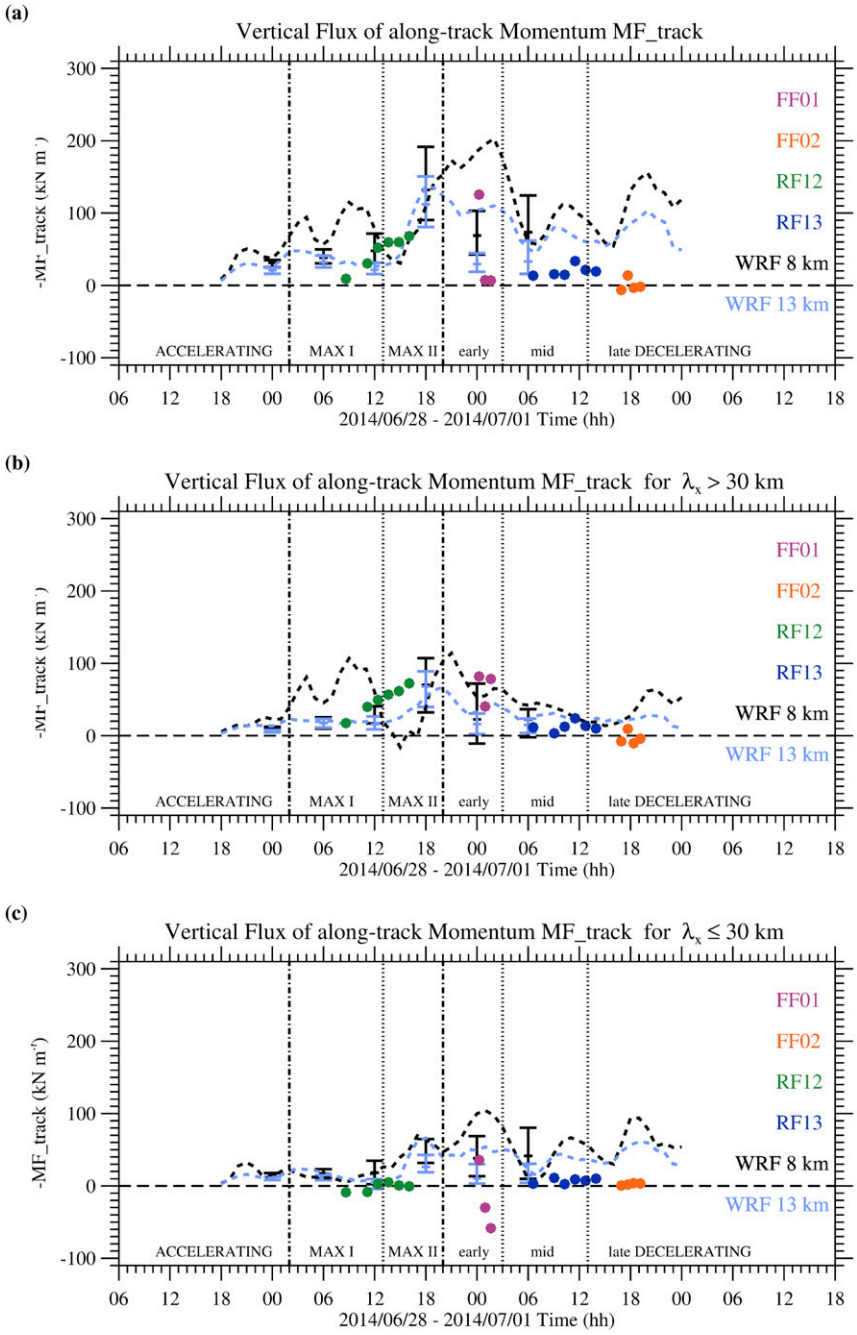

FIG. 11. (a) Time series of leg-integrated vertical flux of along-track momentum ($-MF_{track}$) for the GV (RF12 and RF13) and Falcon (FF01 and FF02) aircraft for all Mt-A-2b legs, as well as of simulated flux values of the WRF Model smoothed over 3 h along the Mt-A-2b transect at typical flight altitudes of 8 and 13 km. As in Figs. 2 and 6, the divisions into accelerating, part I and II of maximum, early, mid-, and late decelerating forcing phases are marked with vertical lines. In addition, minimum, mean, and maximum $-MF_{track}$ values at 8- (black) and 13-km (light blue) altitude of six quasi-steady WRF runs with constant background profiles initialized at 0000, 0600, 1200, and 1800 UTC 29 Jun and at 0000 and 0600 UTC 30 Jun are shown as error bars (also see Fig. 13). (b),(c) As in (a), but only for signal parts including wavelengths larger and smaller than 30 km, respectively.

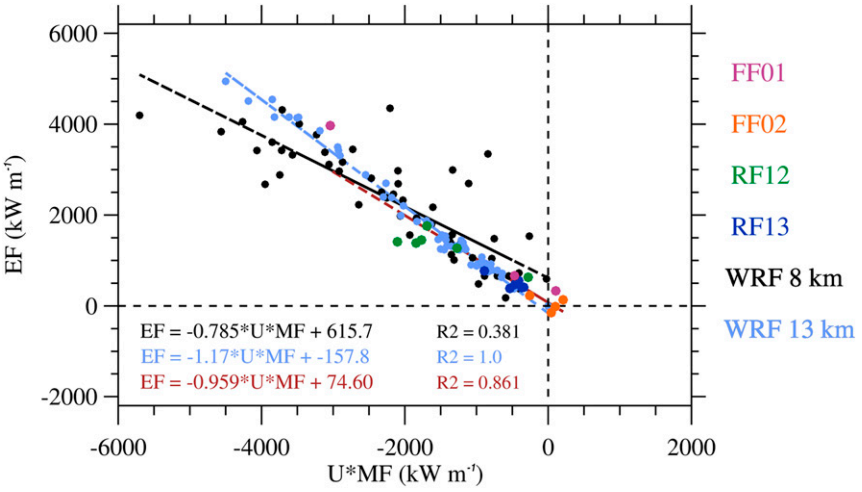

FIG. 12. Test of the linear Eliassen–Palm relation between the energy flux (EF_z) and the scalar product of horizontal wind ($\mathbf{U} = [u, v]$) and the horizontal momentum flux ($\mathbf{MF} = [MF_x, MF_y]$) for all Mt-A-2b legs during IOP 9 and the WRF simulations along the Mt-A-2b transect at 8- and 13-km altitude. The solid lines represent the linear regression of EF_z and $\mathbf{U} \cdot \mathbf{MF}$ for WRF at 8-km altitude (black), at 13-km altitude (light blue), and the airborne observations of the Mt-A-2b legs (red). Further given are the respective functions of the linear regression and the squared Pearson correlation coefficient R^2.

the transition from maximum forcing phase part II to early decelerating forcing phase. Thereafter, stratospheric $-MF_{track}$ fluctuates like the tropospheric $-MF_{track}$, but with lower amplitudes. Generally, stratospheric $-MF_{track}$ values are smaller than the tropospheric values, except a few hours during maximum forcing phase part II.

The simulated $-MF_{track}$ values fairly follow the observed increase of stratospheric $-MF_{track}$ values during RF12 (Fig. 11a). Simulated and observed tropospheric momentum fluxes during FF01 are larger than the stratospheric ones. However, the simulated values are larger by up to 100 kN m^{-1}, compared to the observed ones. The simulations further overestimate $-MF_{track}$ of RF13 and FF02 by more than 30 kN m^{-1}. Despite the quantitative differences of simulated and observed fluxes, their temporal evolutions show increasing fluxes during maximum forcing phase part I, strongest fluxes at the transition from maximum forcing phase part II to early decelerating forcing phase, and lower values thereafter. This temporal evolution reflects a retarded maximum of UTLS fluxes (6–14 h) after the maximum upstream low-level forcing (see Fig. 6).

For linear, steady, nondissipating mountain waves, the Eliassen–Palm relation links the vertical energy flux to the scalar product of horizontal wind **U** and horizontal momentum flux (**MF**): $EF_z = -\mathbf{U} \cdot \mathbf{MF}$ (Eliassen and Palm 1960). Generally, both the observations (colored in Fig. 12) and the WRF simulations at 13-km altitude (light blue) satisfy this linear relation. The slopes of the corresponding linear regressions are near unity, and offsets are relatively small. The largest scatter and lowest Pearson correlation coefficient ($R^2 = 0.38$) occurs for the WRF simulation at 8-km altitude, indicating nonlinear, unsteady processes like wave breaking and wave reflection in the upper troposphere. Deviations from the linear relation mainly occurred in the troposphere during the maximum forcing phase. The observations and the stratospheric WRF simulations, in contrast, reveal less scatter and R^2 values close to 1.

In the following, we investigate if the evolution and magnitude of $-MF_{track}$ during this transient wave event can be described by $-MF_{track}$ values from a series of 2D WRF runs initialized at 0000, 0600, 1200, and 1800 UTC 29 June and at 0000 and 0600 UTC 30 June, respectively. We selected the period from 30- to 48-h lead time to average $-MF_{track}$ values of the 2D simulations and compare these to the $-MF_{track}$ values of the transient run and the observations. In this simulation period, the flow in all 2D runs reaches a quasi-steady state. Intentionally, we use the term ''quasi steady'' to point out that there still might be unsteady effects involved due to wave–wave and wave–mean-flow interactions.

Figure 13 shows the leg-integrated $-MF_{track}$ values of the quasi-steady runs at 13-km altitude as a function of run time after initialization. After a spinup time with maximum fluxes, all runs show decreasing or nearly steady $-MF_{track}$ values. Based on the temporal evolution

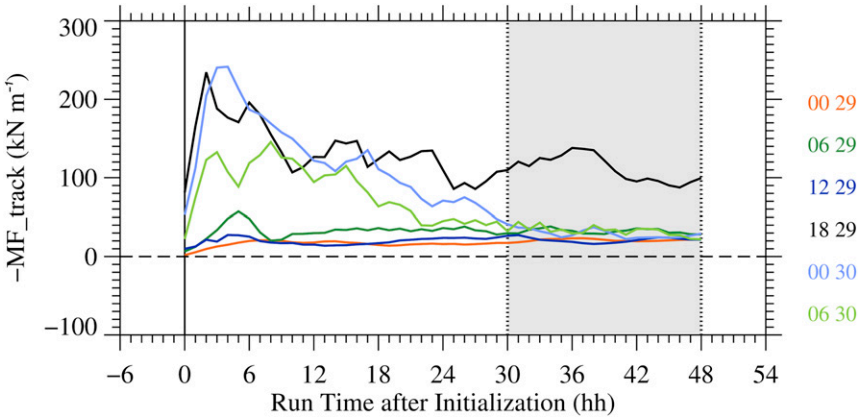

FIG. 13. WRF leg-integrated 3-h-smoothed vertical flux of along-track momentum of quasi-steady runs at 13-km altitude as a function of run time after the respective initialization. All runs were simulated for 48 h. The light gray shading gives the time interval (30–48-h run time) during which the simulations are assumed to reach a quasi-steady state. This time interval is used to average the flux values and to compare to the "transient" WRF simulation and the observations in Fig. 11.

of their $-\mathrm{MF}_{\mathrm{track}}$ values, the six runs can be divided into two groups. The first group is initialized in the accelerating and maximum forcing phases at 0000, 0600, and 1200 UTC 29 June. The second group is initialized in the transition from maximum to decelerating forcing phases at 1800 UTC 29 June and 0000 and 0600 UTC 30 June. The $-\mathrm{MF}_{\mathrm{track}}$ values of the first group rise only a little and reach a quasi-steady state after ≈10-h run time, with $15 < \mathrm{MF}_{\mathrm{track}} < 40\,\mathrm{kN\,m^{-1}}$. In contrast, $-\mathrm{MF}_{\mathrm{track}}$ values of the second group increase to values $>200\,\mathrm{kN\,m^{-1}}$ for the 1800 UTC 29 June and 0000 UTC 30 June runs and to $>100\,\mathrm{kN\,m^{-1}}$ for the 0600 UTC 30 June run. Afterward, the simulated fluxes drop off to values between 1/2 and 1/8 of their individual maxima. Another difference from the earlier runs is that the last three runs later approach their quasi-steady states after ≈30 h (gray shaded in Fig. 13). Momentum fluxes of the runs during the decelerating forcing phase decrease gradually in time.

Error bars with the minimum, mean, and maximum $-\mathrm{MF}_{\mathrm{track}}$ values of the quasi-steady runs at 8- and 13-km altitude were computed within 30–48 h after their initializations and are added in Fig. 11a. The three quasi-steady runs initialized in the accelerating and maximum forcing phases reproduce the observed and simulated low stratospheric fluxes, but show smaller values than the transient run by 10 to 20 $\mathrm{kN\,m^{-1}}$ for the troposphere. The largest $-\mathrm{MF}_{\mathrm{track}}$ values among all quasi-steady runs are simulated by the 1800 UTC 29 June run initialized at the end of the maximum forcing phase. These values compare well with those of the fully transient run. The run initialized in the early decelerating forcing phase at 0000 UTC 30 June shows lower tropospheric values than the transient run for this time and lower values than the observation of FF01 leg 2 (first violet dot in Fig. 11). At 13-km altitude, this run and the later run initialized at 0600 UTC 30 June also have lower flux values than the transient run, but their values fit better to the stratospheric observations of FF01 and RF13, compared to the transient run. Generally, the three runs of the first group show a smaller spread between minima und maxima than the runs of the second group. According to this comparison, the evolution of the observed $-\mathrm{MF}_{\mathrm{track}}$ in the lower stratosphere from the maximum forcing phase to the mid-decelerating forcing phase largely follows a sequence of fluxes simulated by individual quasi-steady runs initialized in the same forcing phases.

3) MOMENTUM-CARRYING WAVE SCALES

The amount of wave momentum carried by gravity waves depends on the horizontal wavelength λ_x (Smith et al. 2016). Figures 11b and 11c show $-\mathrm{MF}_{\mathrm{track}}$ calculated for perturbations u'_{track} and w' associated with large-scale ($\lambda_x > 30$ km) and small-scale ($\lambda_x \leq 30$ km) waves as reconstructed by the wavelet analysis, respectively. A value of $\lambda_x = 30$ km is an appropriate cutoff wavelength for the small-scale contributions, as the analyzed airborne data reveal a minimum of wave momentum and energy around $30 < \lambda_x < 60$ km (not shown). Therefore, wave momentum and energy contributions of $\lambda_x > 30$ km can be equated to those of $\lambda_x > 60$ km. The contributions of large-scale (Fig. 11b) and small-scale waves (Fig. 11c) to the leg-integrated momentum flux $-\mathrm{MF}_{\mathrm{track}}$ evolve differently in time. In the following, we present the individual forcing phases step by step.

The peaks in the total simulated tropospheric $-\mathrm{MF}_{\mathrm{track}}$ during the maximum forcing phase part I (Fig. 11a) can be attributed to long waves with $\lambda_x > 30$ km (Fig. 11b). Afterward, these tropospheric flux values decrease and reach even negative values around 1500 UTC. Similar to the observed stratospheric fluxes with $\lambda_x > 30$ km, the simulated fluxes increase until the transition from maximum to decelerating forcing phase. However, the observed values are about 20–30 kN m^{-1} larger than the simulated one, except for the first RF12 leg. Observed and simulated waves with $\lambda_x \leq 30$ km only marginally contribute to the total flux in the UTLS (Fig. 11c) during this period. In the beginning of the maximum forcing phase part II, the WRF simulation already shows increasing small-scale wave activity, whereas the observations still give around zero flux values, as illustrated by the last two legs of RF12 (Fig. 11c).

During the transition from maximum to decelerating forcing phase, both short and long waves contribute to the broad peaks of the total simulated $-\mathrm{MF}_{\mathrm{track}}$ by about 110 kN m^{-1} for 8-km altitude and by 65 kN m^{-1} for 13-km altitude, respectively, as visible in Figs. 11b and 11c. As in the preceding maximum forcing phase, the observations in the early decelerating forcing phase exhibit higher flux values for $\lambda_x > 30$ km than the simulations, except for one leg (Fig. 11b). For the small-scale waves, observed fluxes are about half the simulated values in the troposphere (first violet dot in Fig. 11c). The observed momentum flux carried by waves with $\lambda_x \leq 30$ km even reverses sign in the stratosphere (last two violet dots in Fig. 11c), which is not found in the simulation.

During the mid-decelerating forcing phase, both simulations and observations reveal a trend of decreased fluxes of large-scale waves with about similar values. Apparently, the excitation of long waves has ceased since the beginning of the decelerating forcing phase. Therefore, the oscillating character of the total simulated $-\mathrm{MF}_{\mathrm{track}}$, as visible in Fig. 11a, during the mid- and late decelerating forcing phases results from small-scale wave activity. Obviously, the simulated $-\mathrm{MF}_{\mathrm{track}}$ of small-scale waves is overestimated, compared to the observations of RF13 and FF02 (Fig. 11c). Wagner et al. (2017) explain this overestimation with a lack of turbulent diffusion in the WRF simulation.

The wavelength decomposition of $-\mathrm{MF}_{\mathrm{track}}$ of the quasi-steady runs also reveals intensifying large-scale wave activity toward the transition from maximum to decelerating forcing phase (error bars in Fig. 11b). Thereafter, decreasing flux values are simulated for $\lambda_x > 30$ km. The evolution of the stratospheric flux values of the transient run for $\lambda_x > 30$ km can be represented by the individual quasi-steady runs, as the stratospheric $-\mathrm{MF}_{\mathrm{track}}$ values of the fully transient run are covered by the variability (error bars) of the quasi-steady runs. As for the fully transient run, these simulated values of the 2D quasi-steady runs are mostly smaller than the observed values. The range of tropospheric $-\mathrm{MF}_{\mathrm{track}}$ values of the first group of quasi-steady runs is smaller than $-\mathrm{MF}_{\mathrm{track}}$ values of the fully transient run. The second group of quasi-steady runs, with its larger spread between minima and maxima, better captures the flux values of the fully transient simulation.

Transiently simulated and observed flux values for $\lambda_x \leq 30$ km lie within the range of the error bars for the first group of the quasi-steady runs in both the troposphere and the stratosphere (Fig. 11c). The small-scale flux values of the second group differ from the observations and the fully transient simulation, except for the stratospheric values of the last quasi-steady run at 0600 UTC 30 June. The largest difference between observed and quasi-steady fluxes appears during the early decelerating forcing phase, when fluxes of reversed sign for the small-scale waves are detected in the stratosphere.

Summarizing, the long waves dominate the transient behavior in the stratosphere. Observations reveal that the small-scale wave contributions have small flux values and do not vary much in time. Large positive and large negative flux values of the small-scale waves occur in the troposphere and stratosphere, respectively, during the early decelerating forcing phase. The WRF simulations are able to represent the general evolution of the large-scale component, whereas the small-scale contributions are overestimated.

4) Local scale-dependent fluxes

The previous analysis concentrated on the temporal evolution of the leg-integrated along-track momentum fluxes. Next, the extended wavelet transform, as described in the appendix, is applied to quantify the horizontal wavelengths associated with locations of significantly enhanced (5% significance level) vertical energy flux $\mathrm{EF}_{z_n}(s_j)$ and along-track momentum flux $\mathrm{MF}_{\mathrm{track}_n}(s_j)$. Based on the respective signs of the spectral amplitudes of $\mathrm{MF}_{\mathrm{track}_n}(s_j)$ and $\mathrm{EF}_{z_n}(s_j)$, the dominant vertical propagation direction of wave packets (from linear, steady-state theory) was determined along selected GV and Falcon flight legs.

During the maximum forcing phase part I, the GV RF12 leg 6 (at around 12-km altitude) is dominated by positive spectral amplitudes of $0.1 < \mathrm{EF}_{z_n}(s_j) < 0.3$ kW m^{-1} at horizontal wavelengths between 40 and 120 km. These values are statistically significant in the range $60 \lesssim \lambda_x \lesssim 80$ km and are located over the main ridge of the Southern Alps (Fig. 14a). The spatial coincidence of the spectral peaks of negative momentum

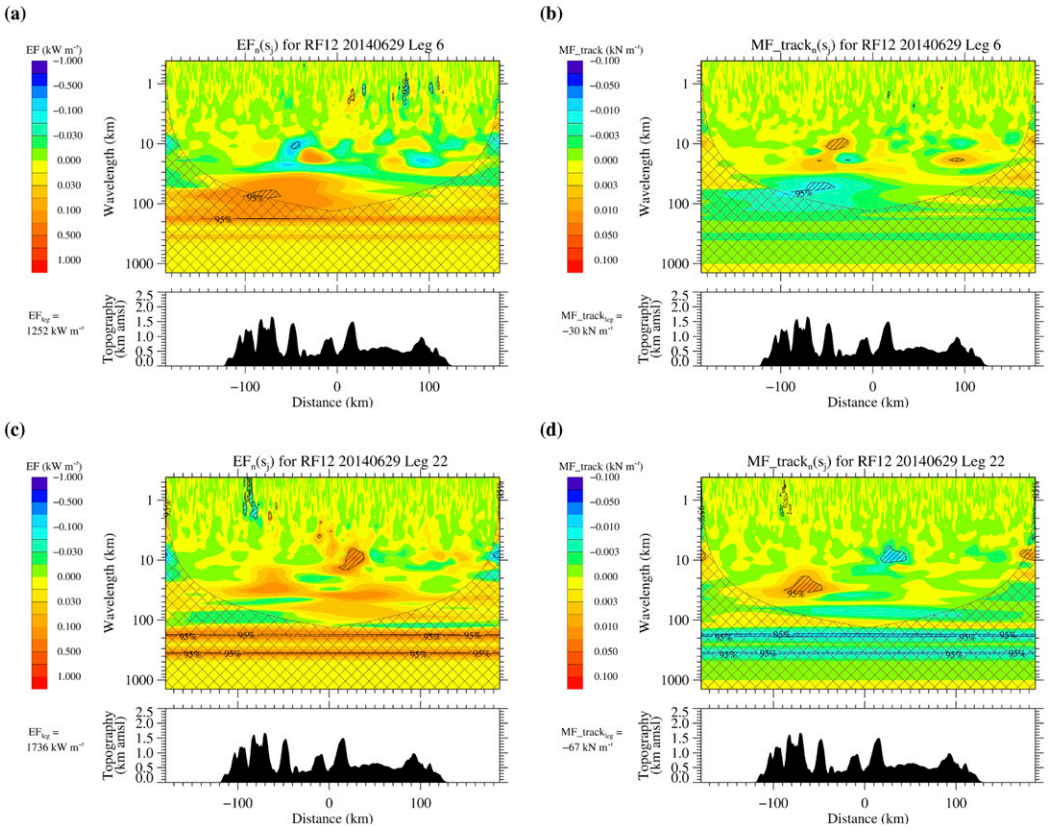

FIG. 14. (a) $EF_{z_n}(s_j)$ (vertical energy flux) and (b) $MF_{track_n}(s_j)$ (along-track momentum flux) wavelet cospectra with underlying topography for the GV RF12 leg 6 on 29 Jun 2014 during maximum forcing phase of the IOP 9. The hatched area is significant on the 5% level, and the surrounding solid black line represents the 95% confidence limit. The cross-hatched area gives the cone of influence. (c),(d) As in (a),(b), but for GV RF12 leg 22.

flux $-0.01 < MF_{track_n}(s_j) < -0.007$ kN m^{-1} (slightly shifted downstream and to smaller wavelengths) with the $EF_{z_n}(s_j) > 0$ pattern suggests an upward-propagating gravity wave with $\lambda_x \approx 60$–70 km (Fig. 14b). The location and the wave scale are in agreement with the dominating signal of the vertical displacements in Fig. 10a. Another significant region in both cospectra with $\lambda_x \approx 10$ km is located over Mt. Alta at −45-km distance. In contrast to the former region, here, negative spectral amplitudes of $-0.3 < EF_{z_n}(s_j) < -0.1$ kW m^{-1} coincide with positive momentum fluxes of $0.007 < MF_{track_n}(s_j) < 0.01$ kN m^{-1}, suggesting a downward-propagating gravity wave.

In the maximum forcing phase part II, the GV detected strong turbulence along the flight leg 22 (altitude of 13.5 km) above the main mountain range between −100- and −80-km distance (Figs. 14c,d). This enhanced turbulence is reflected by significant flux values in the wavelength range 400 m $\lesssim \lambda_x \lesssim$ 2 km. During the same flight leg and at approximately the same location, enhanced spectral amplitudes with $0.1 < EF_{z_n}(s_j) < 0.3$ kW m^{-1} and $0.01 < MF_{track_n}(s_j) < 0.03$ kN m^{-1} [significant in $MF_{track_n}(s_j)$] are found at $\lambda_x \approx$ 30 km (Figs. 14c,d). The same sign of $EF_{z_n}(s_j)$ and $MF_{track_n}(s_j)$ excludes vertically propagating linear waves. The superposition of longer and shorter spectral components suggests local wave breaking in the lower stratosphere at this location. During the same GV flight leg 22, linear upward-propagating mountain waves with $10 \lesssim \lambda_x \lesssim 20$ km were detected above the Dunstan Mountains at about 20-km distance, with significant spectral amplitudes of $0.3 < EF_{z_n}(s_j) < 0.5$ kW m^{-1} and $-0.03 < MF_{track_n}(s_j) < -0.01$ kN m^{-1} (Figs. 14c,d). This is the first detection of upward-propagating gravity waves over the Dunstan Mountains during the maximum forcing phase, 7 h after the beginning of airborne observations.

During the early decelerating forcing phase, the Falcon flight FF01 observed strong, upward-propagating mountain waves in leg 2 (8 h later than GV leg 22), with $EF_{z_n}(s_j) > 1$ kW m^{-1}, $-0.05 < MF_{track_n}(s_j) < -0.03$ kN m^{-1}, and $12 \lesssim \lambda_x \lesssim 35$ km wavelength in the upper troposphere

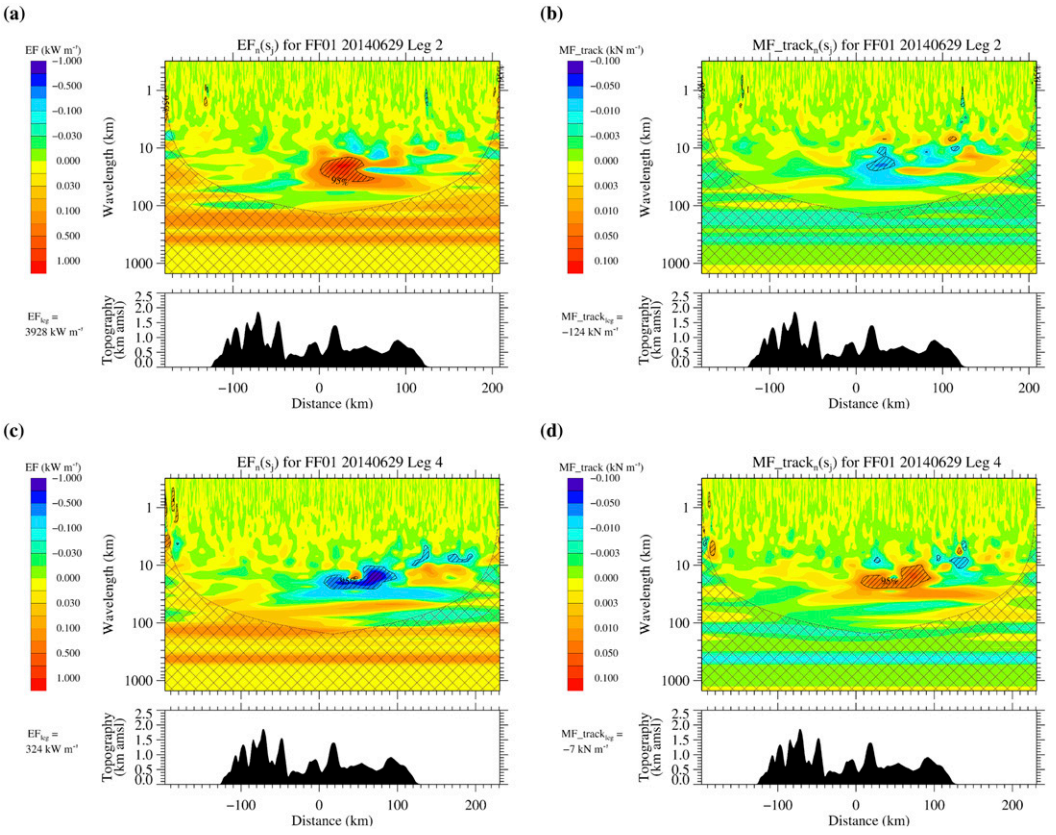

FIG. 15. (a),(b) and (c),(d) As in Figs. 14a and 14b, respectively, but for Falcon FF01 leg 2 on 29 Jun and leg 4 on 30 Jun 2014 during early decelerating forcing phase of the IOP 9.

also above the Dunstan Mountains at ≈20-km distance (Figs. 15a, b). Here, the enhanced spectral amplitudes extend about 50 km downwind from the Dunstan Mountains. Along the same flight track, about 1 h later and 1 km higher than the previous flight leg 2, large negative energy flux values of $-1 < \mathrm{EF}_{z_n}(s_j) < -0.7$ kW m^{-1} and large positive momentum flux values of $0.05 < \mathrm{MF}_{\mathrm{track}_n}(s_j) < 0.07$ kN m^{-1} indicate large-amplitude, downward-propagating gravity waves above and downstream of the Dunstan Mountains (Figs. 15c,d).

The mid- and late decelerating forcing phases were already characterized by considerably decreased wave amplitudes observed during RF13 and FF02, as described above for the leg-integrated fluxes (Fig. 11a) and the vertical displacements (Figs. 10c,d). At around 9-km altitude within the tropopause, positive smaller energy flux values of $0.1 < \mathrm{EF}_{z_n}(s_j) < 0.3$ kW m^{-1} with $\lambda_x \approx 18$ km and $\lambda_x \approx 30$ km of the FF02 leg 2 stretch between the Dunstan Mountains and the Mt. Pisgah range (Fig. 16a). The fair consistency with collocated significant negative momentum flux values of $-0.007 < \mathrm{MF}_{\mathrm{track}_n}(s_j) < -0.003$ kN m^{-1} indicates weak upward-propagating waves (Fig. 16b). But downward-propagating waves were also identified by the wavelet analysis at this stage of the transient evolution. Two negative significant energy flux patches of $-0.07 < \mathrm{EF}_{z_n}(s_j) < -0.03$ kW m^{-1} at $\lambda_x \approx 10$ km exist in the lee of the SI. They appear at the same spatial location as a significant positive momentum flux signature of $0.003 < \mathrm{MF}_{\mathrm{track}_n}(s_j) < 0.007$ kN m^{-1}.

The subsequent leg 3 of FF02 was conducted at around 10.5-km altitude above the tropopause. The Falcon observed a significant upward-propagating wave of 20–30-km wavelength, with $0.1 < \mathrm{EF}_{z_n}(s_j) < 0.3$ kW m^{-1} and $-0.03 < \mathrm{MF}_{\mathrm{track}_n}(s_j) < -0.01$ kN m^{-1} directly above and downstream of the Dunstan Mountains (Figs. 16c,d). Smaller patches of downward-propagating waves with $-0.3 < \mathrm{EF}_{z_n}(s_j) < -0.1$ kW m^{-1}, $0.003 < \mathrm{MF}_{\mathrm{track}_n}(s_j) < 0.007$ kN m^{-1}, and $\lambda_x \approx 12$ km appear at around −10- and 100-km distance. Not only over the Dunstan Mountains, but also upstream at around −60-km distance, an upward-propagating wave with significant positive energy flux values of $0.1 < \mathrm{EF}_{z_n}(s_j) < 0.3$ kW m^{-1} and significant negative momentum flux values of $-0.007 < \mathrm{MF}_{\mathrm{track}_n}(s_j) < -0.003$ kN m^{-1} can be observed over the Mt. Aspiring massif. During this late decelerating forcing phase, small-amplitude

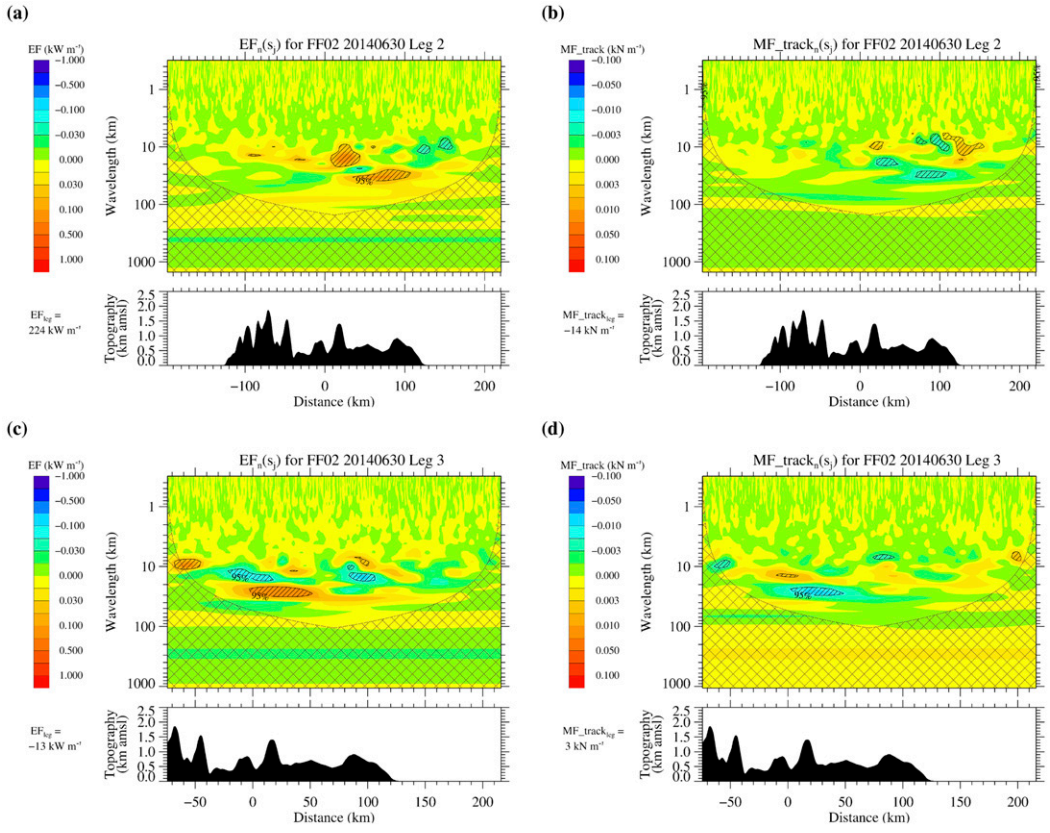

FIG. 16. (a),(b) and (c),(d) As in Figs. 14a and 14b, respectively, but for Falcon FF02 legs 2 and 3 on 30 Jun during late decelerating forcing phase of the IOP 9. Note the different limits of the distance axis for leg 3 in (c),(d).

short waves between 9- and 30-km wavelength thus dominate over the Dunstan Mountains, the Mt. Aspiring range, and the Mt. Pisgah range, that is, all outstanding peaks along the Mt-A-2b cross section. In contrast to the previous Falcon flight FF01, there are no remarkable differences between wave signatures at the upper-tropospheric and the lower-stratospheric flight levels.

Previously identified contributions of small-scale and large-scale waves [section 4a(3)] to leg-integrated fluxes were now attributed to different mountain peaks and ranges. Upward-propagating large-scale waves were detected only during the maximum forcing phase over the main mountain ridge. Small-scale waves with larger flux values dominated the decelerating forcing phase. Because of downward-propagating waves, leg-integrated fluxes are small or even of reversed sign at stratospheric levels in the decelerating forcing phase.

b. Vertical propagation into the mesosphere

As mentioned above (section 3), the vertical wave propagation during the maximum forcing phase part I is influenced by the existence of a low-stability layer associated with the passing STJ. To illustrate this effect, we show approximated and density-corrected vertical velocity perturbations w' obtained from the balloon ascent rates, calculated according to Reeder et al. (1999) and Lane et al. (2000). The 1129 UTC sounding has large peak-to-peak amplitudes up to $4\,\mathrm{m\,s^{-1}}$ in the lower and midtroposphere (Fig. 17a). Above, in the UTLS, the amplitudes are damped to less than a quarter of their tropospheric value. The altitude of the damping coincides with the low-stability layer in the range $9 \lesssim z \lesssim 11$ km, which is marked by the almost-vertical potential temperature profile, resulting in a frequent occurrence of layers with $-0.06 < \partial\theta/\partial z < 0.09\ \mathrm{K\,km^{-1}}$ in the upper troposphere (black line and gray shaded layers in Fig. 17a). Also, as shown by our Fig. 2 and by Fig. 4 of Gisinger et al. (2017) the strength of the TIL is enhanced in this period. An increased hydrostatic reflection coefficient r up to 0.57 was documented in Fig. 5 in Gisinger et al. (2017). Linear theory predicts that the net upward energy flux is $(1 - r^2)$ times the flux of the incident wave (Eliassen and Palm 1960). The hydrostatic reflection coefficient (Eliassen and Palm 1960) can be calculated for large Richardson numbers ($\mathrm{Ri} \gg 1/4$), that is, no or negligible vertical shear, according to

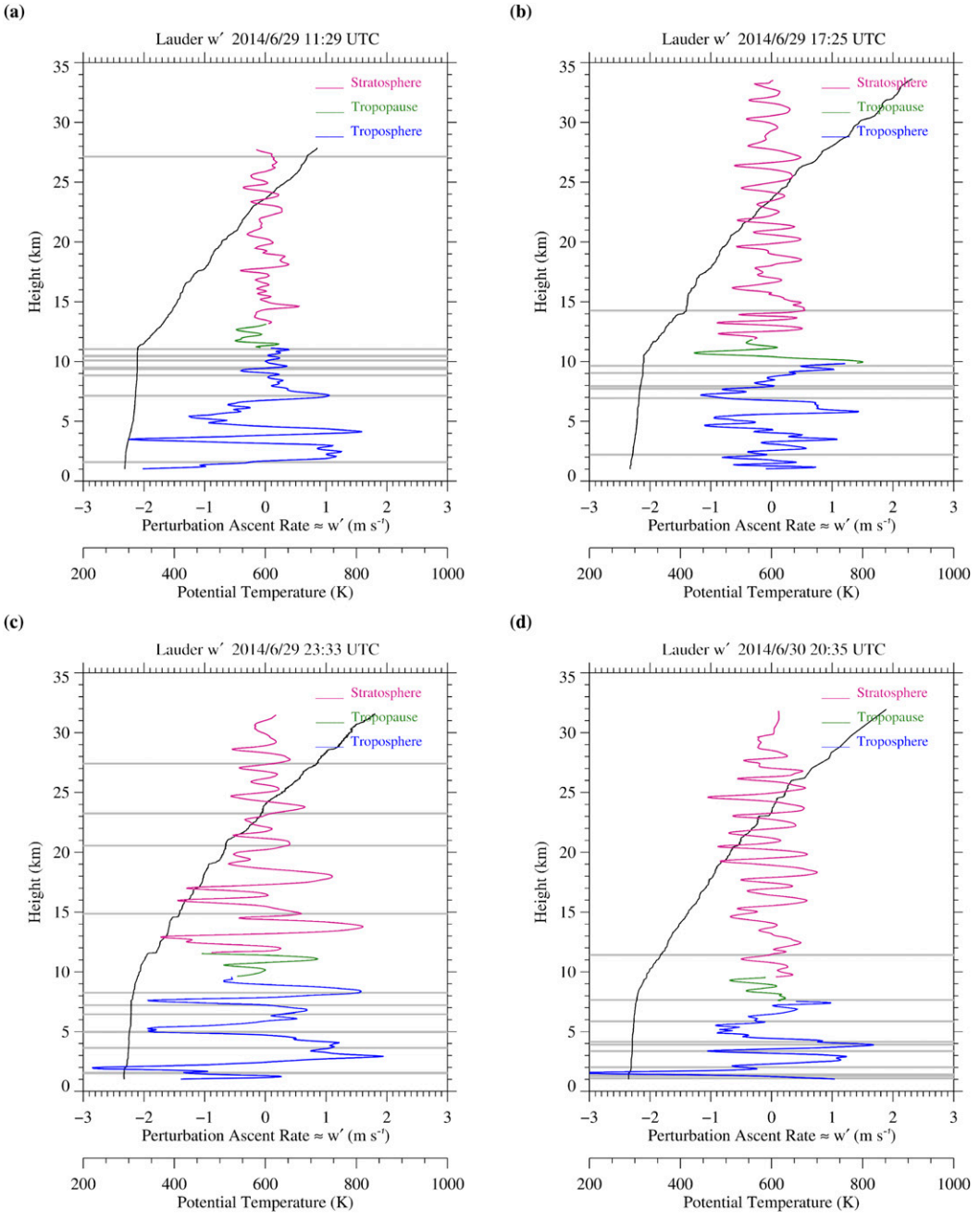

FIG. 17. Density-corrected, approximated vertical velocity fluctuation and potential temperature of the radiosoundings launched at Lauder at (a) 1129 UTC (maximum forcing phase part I), (b) 1725 UTC (maximum forcing phase part II), and (c) 2333 UTC 29 Jun (early decelerating forcing) and at (d) 2035 UTC 30 Jun (late decelerating forcing). Density-corrected refers to the multiplication of w' by the factor $[\rho(z)/\rho(z=0)]^{1/2}$ to remove the effect of exponentially amplifying w' with height due to decreasing density ρ. The flight passages within the troposphere, tropopause, and stratosphere are colored in blue, green, and violet, respectively. Gray shaded are layers where $-0.06 < \partial\theta/\partial z < 0.09$ K km^{-1}.

$r \approx [(N_S - N_T)/(N_T + N_S)]$, where N_T and N_S are the representative mean Brunt–Väisälä frequencies of the troposphere and the stratosphere, respectively (Keller 1994). The low-stability layer in the upper troposphere (i.e., a small N_T) thus results in a larger r, less net upward energy flux (downward momentum flux), and damped amplitudes above. Therefore, further aloft, the w' amplitudes remain small (Fig. 17a).

During the maximum forcing phase part II, w' amplitudes are reduced within the troposphere (1725 UTC Lauder sonde, cf. Fig. 17b), compared to the former sounding. However, the w' amplitudes have doubled in the entire stratosphere in comparison to those during maximum forcing phase part I (1129 UTC radiosonde, Fig. 17a). Also, the vertical gradient of potential temperature has increased in the upper troposphere, giving higher values of N_T (fewer gray-shaded layers of $-0.06 < \partial\theta/\partial z < 0.09$ K km^{-1} in Fig. 17b). This reduces the difference between the maximum of N and its tropospheric value. In agreement with the observed increase of N_T, the simulated TIL has weakened in strength (Fig. 2), and the hydrostatic reflection coefficient is reduced to around 0.5 during this period [Fig. 5 in Gisinger et al. (2017)]. The increasing penetrability of the upper troposphere coincides with the downstream advection of the low-stability layer during the maximum forcing phase part II (section 3, Fig. 8b). Furthermore, wave breaking is indicated by a nearly adiabatic layer at about 14-km altitude, also gray shaded in Fig. 17b as $-0.06 < \partial\theta/\partial z < 0.09$ K km^{-1}, which is located in the minimum wind layer between the peaks of the double jet (Fig. 8a).

During the early decelerating forcing phase, large-amplitude vertical velocity fluctuations of, on average, ± 1.5 m s^{-1} exist within the troposphere and extend up to around 19-km altitude (2333 UTC 29 June Lauder sonde; cf. Fig. 17c). Below 19-km altitude, wave amplitudes decrease slightly with altitude, attaining mean peak-to-peak amplitudes of around 3 m s^{-1}. Above, peak-to-peak wave amplitudes are more strongly attenuated to around 1 m s^{-1}. The horizontal projection technique of Lane et al. (2000) was applied to determine the horizontal and vertical wavelengths of the large-amplitude signal of the 2333 UTC 29 June sounding: this reveals a horizontal wavelength of around 10 km with a vertical wavelength varying around 4–8 km in the stratosphere.

Another remarkable finding of the radiosounding at 2333 UTC 29 June 2014 is the distinct staircase structure of the potential temperature profile in the stratosphere (Fig. 17c). The staircase structure is further quantified by detecting several stratospheric layers where $-0.06 < \partial\theta/\partial z < 0.09$ K km^{-1} (gray shaded in Fig. 17c) that were not present during the former soundings. Such a profile with frequent occurrence of $\partial\theta/\partial z \approx 0$ in the stratosphere indicates a sequence of vertically stacked mixing layers.

In the sounding launched during the late decelerating forcing phase (2035 UTC 30 June Lauder sonde), the vertical velocity fluctuations show locally strong wave excitation at the ground, but decreasing amplitudes around the tropopause (Fig. 17d). Further aloft, w' is recorded with regular fluctuations and with, on average, larger amplitudes of ± 0.5 m s^{-1} than below. In comparison to the former 2333 UTC 29 June sounding, a staircase behavior of the potential temperature profile is still observed, especially between 20- and 27-km altitude, but $\partial\theta/\partial z$ has generally increased, and no gray-shaded layers exist above 12-km altitude in Fig. 17d.

These soundings during the different forcing phases especially illustrated the effects of the changing propagation conditions. The soundings could prove the strong damping character of the low-stability layer in the upper troposphere (Fig. 17a) and could identify the minimum wind layer between the peaks of the double jet as a mixing region (Fig. 17b). Stratospheric wave activity increased from the maximum forcing phase to early decelerating forcing phase. During the latter phase, wave-breaking layers were found in the stratosphere between about 15- and 25-km altitude (Fig. 17c). Thereafter, stratospheric wave activity decreased (Fig. 17d).

As was indicated by the 2333 UTC 29 June radiosounding, attenuated gravity waves existed above the gravity wave breaking layers from ≈15- to ≈24-km altitude during the early decelerating forcing phase. Hence, the question arises if orographic gravity wave activity is observed even further aloft. A measure of stratospheric and mesospheric gravity wave activity is given by the GWPED, calculated from temperature fluctuations of the Rayleigh lidar measurements from Lauder (Fig. 18). Nine hours of measurements on 30 June 2014 show a transient behavior. In particular, the mesospheric gravity wave activity reached peak values of GWPED of around 110 J kg^{-1} between 1500 and 1600 UTC in the decelerating forcing phase. The stratospheric gravity wave activity is continually decreasing, from a GWPED maximum of about 30 J kg^{-1} at around 1130 UTC to 5 J kg^{-1} at around 1930 UTC. The stratospheric and mesospheric maxima, with a plateau of wave activity in the stratopause in between, are time shifted by around 4 h. Assuming an upward propagation of hydrostatic mountain waves, the propagation time $t_p = \Delta z/c_{gz}$ with $c_{gz} = \langle U_h \rangle_z^2 k/\langle N \rangle_z$ (see Gill 1982; Dörnbrack et al. 1999) can be estimated to around 12 h from the UTLS up to the mesosphere ($\Delta z = 60$ km), with $\lambda_x \approx 200$ km, $\langle N \rangle_z \approx 0.02$ s^{-1}, and $\langle U_h \rangle_z \approx 30$ m s^{-1}, where $\langle\,\rangle_z$ denotes an average over the vertical range. Counting back from the maximum mesospheric GWPED at 1500 UTC 30 June, the resulting time is close to the maximum of long-wave activity in the early decelerating forcing phase (Figs. 10b, 11b).

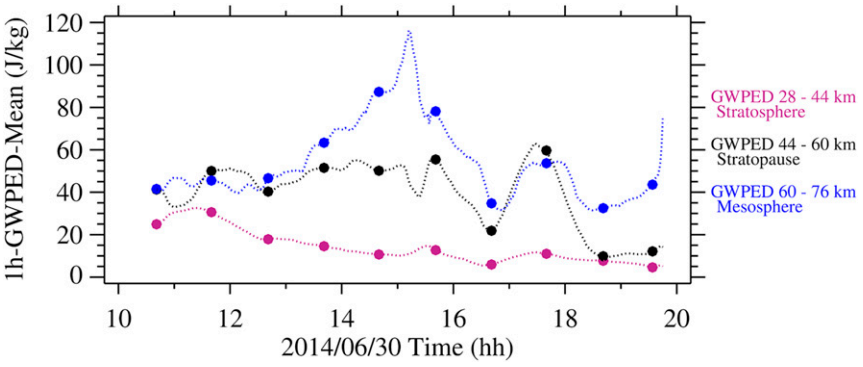

FIG. 18. One-hourly mean of GWPED, logarithmically averaged over the upper stratosphere (violet dots), stratopause (black dots), and mesosphere (blue dots). In addition, the thin dotted lines denote the 1-hourly running mean of the 2-min GWPED data during the Rayleigh lidar measurement at Lauder, NZ, on 30 Jun. In general, the GWPED increases with height due to wave amplification with decreasing air density.

Airborne AMTM observations obtained during the two GV research flights RF12 and RF13 on 29 and 30 June, respectively, confirm the delayed appearance of those long mountain waves in the mesosphere: while the observations of RF12 during the maximum forcing phase show no clear large-scale structures above the SI (≈1100 UTC 29 June; Fig. 19a), the airglow observations of RF13 reveal elongated maxima of the airglow brightness temperatures parallel to the main mountain ridge and a minimum directly above the SI (≈1400 UTC 30 June; Fig. 19b). The estimated horizontal wavelength amounts to about 200 km and agrees with λ_x estimated from the vertical displacements in the UTLS during the early decelerating forcing phase (Fig. 10b). Counting back with a calculated propagation time of 15 h from 12- to 87-km altitude matches the time of maximum long-wave response in the UTLS (Figs. 10b, 11b). Temperature perturbations and vertical displacements have the same wavenumber dependency in the Fourier space (Smith and Kruse 2017) and are thus comparable in their wave spectrum. It must be noted that the large-scale wave in AMTM appeared only during the last legs of RF13. Summarizing, the deep upward propagation of long hydrostatic mountain waves with $\lambda_x \approx 200$ km, which were observed in the UTLS during the early decelerating forcing phase, up to the mesosphere,

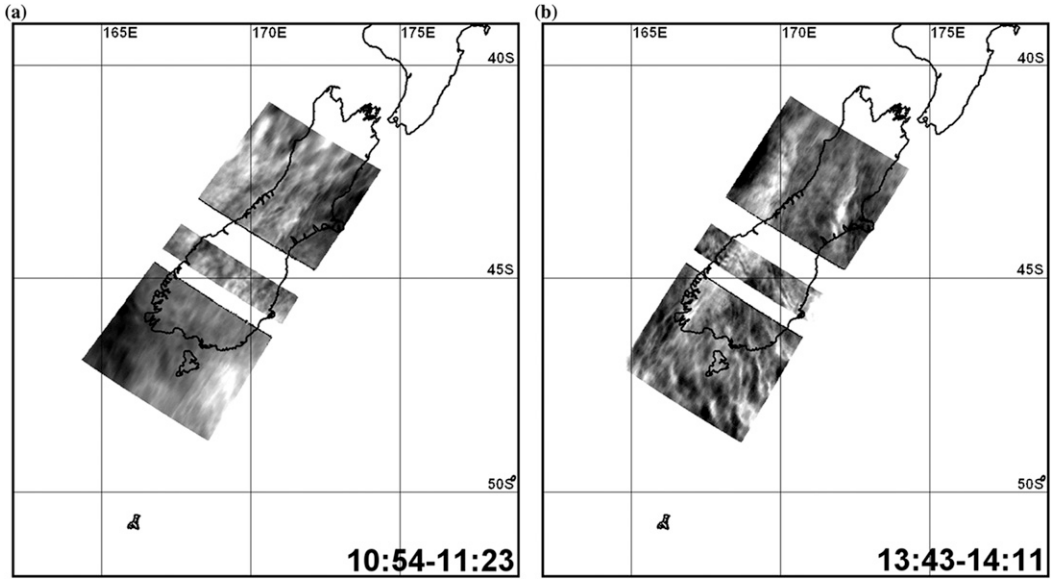

FIG. 19. Keograms (time–distance sections constructed from collocated time series of narrow AMTM image slices) of the AMTM observations during (a) RF12 on 29 Jun and (b) RF13 on 30 Jun 2014.

is identified by combining airborne data from flight level and the middle atmosphere.

5. Comparison with previous studies and discussion

In this section, we discuss our results in the context of numerical studies of transiently forced mountain waves, as well as in the context of previous investigations of MAP, T-REX, and DEEPWAVE studies.

A detailed and quantitative comparison of our findings for this complex transient wave event with existing theoretical and idealized numerical simulation studies (Lott and Teitelbaum 1993a,b; Chen et al. 2005, 2007) is hardly possible. The analyzed wave event is not only influenced by transient tropospheric forcing, but also by changing propagation conditions in the UTLS region. Previous studies focused on mountain waves generated during only transient tropospheric forcing (Lott and Teitelbaum 1993a,b; Chen et al. 2005, 2007). In these studies, forcing and propagation conditions varied temporarily at all altitudes in the same way. In contrast, our case study reveals the importance of the varying propagation conditions. They include the passing upper-tropospheric low-stability layer with a correspondingly strong TIL, the double peak structure of the STJ, and the wave breaking in the UTLS and in the stratospheric wind minimum. Nevertheless, the observed temporal dependence of the low-level cross-mountain flow, with an approximated $\cos^2$ variation over about 53 h and a total increase of cross-mountain wind of $\approx 20\,\mathrm{m\,s^{-1}}$, corresponds to values used in those theoretical and numerical studies.

The low-stability layer in the upper troposphere (Fig. 2) occurred in the maximum forcing phase part I and resulted in decreasing values of the Scorer parameter ℓ and large λ_{crit} values of about 30 km (Fig. 8b). As a result, the strength of the TIL and the reflection coefficient r for hydrostatic gravity waves increased. In effect, the stratospheric wave amplitudes were strongly attenuated, as documented by the radiosonde observation (Fig. 17a) and the simulated vertical wind (Fig. 9a). The numerical results reveal that longer waves with $\lambda_x \approx 60$ km were damped, too: a pair of strong down- and updrafts in the lee of the main mountain ridge between −90- and −40-km distance is effectively attenuated in the upper troposphere (Fig. 9a). These findings are confirmed by the small simulated and observed stratospheric momentum fluxes in the maximum forcing phase part II for $\lambda_x > 30$ km in Fig. 11b.

Another peculiarity of the time-varying propagation conditions in the UTLS is the wave breaking between the double peaks of the STJ. There, the cross-mountain wind was reduced by $15\,\mathrm{m\,s^{-1}}$ over less than 2-km altitude (second shaded area in Figs. 8a, 17b). Radiosonde observations revealed a mixing layer in this minimum wind layer (Fig. 17b). As the GV flew within this layer, the observed nonlinearity and turbulence at flight level (Figs. 14c,d) suggests mountain wave breaking. Because of this wave breaking, the observed leg-integrated momentum fluxes for $\lambda_x \leq 30$ km remain negligible (Fig. 11c). This double-jet-induced wave breaking has not been observed previously. However, the occurrence of gravity wave breaking in a layer of negative shear above a tropopause jet was already reported by Doyle et al. (2011) and Smith et al. (2016) during T-REX and other IOPs of the DEEPWAVE campaign.

Vertically stacked mixing layers observed in the stratospheric wind minimum by the radiosounding during the early decelerating forcing phase (Fig. 17c) coincide with simulated wave breaking. The simulated wave breaking and the resulting mixing is indicated by steep isentropes at around 17-km altitude (Fig. 9c). Interestingly, downward-propagating waves in the lower stratosphere were detected in the flight-level data during this period (Figs. 15c,d). The similarity of the horizontal wavelength band and the same location of upward- (leg 2, Figs. 15a,b) and downward- (leg 4, Figs. 15c,d) propagating signals suggest that the observed downward-propagating wave results from partial wave reflection by the breaking region located above the flight leg. Observations of downward-propagating waves extend further into the late decelerating forcing phase (Fig. 16). The numerical simulations support the assumption of reflected mountain waves in this phase, too, as a gravity wave-breaking region is present in the stratospheric wind minimum near 19-km altitude (Fig. 9d). Upward- and downward-propagating waves influence the wave response at the subjacent stratospheric flight levels in such a way that the observed leg-integrated momentum fluxes become negligible (Fig. 11). The observational and numerical evidence of the existence of a stratospheric gravity wave-breaking layer confirms the findings of the so-called ''valve'' layer within the stratospheric wind minimum (Kruse et al. 2016). This valve layer attenuates upward-propagating waves when wave breaking occurs. Indeed, attenuated waves were observed above, indicating a leakage of wave energy into the upper stratosphere during IOP 9 (Figs. 9c, 17c). In general, the existence of the stratospheric wind minimum is not related to the transient mountain-wave event, but to the location of NZ and the seasonal shift of the PNJ (Fritts et al. 2016). The valve layer as a breaking layer depends on the amplitudes of waves that are able to propagate beyond the UTLS in comparison to the magnitude of the stratospheric wind (Kruse et al. 2016). As

wave amplitudes in the lower stratosphere are largest during the early decelerating forcing phase, wave breaking in the stratospheric valve layer was mainly limited to this phase. Therefore, the appearance of the valve is also transient.

Kruse and Smith (2015) classified observed mountain-wave cases of the DEEPWAVE campaign into shallow and deep events, depending on the reduction of horizontal stratospheric wind by 20 or 10 $m\,s^{-1}$, respectively, from a lower-stratospheric value of 30 $m\,s^{-1}$. Based on this classification, the reduction of $U_{\perp}$ ($\approx U_{hor}$ at this time and altitude region) from 30 $m\,s^{-1}$ at 14-km altitude to 16 $m\,s^{-1}$ at 17-km altitude (green line in Fig. 8a) places our event in between the characteristic values of shallow and deep gravity wave propagation. Essentially, both wave attenuation and leakage of wave energy into the upper atmosphere characterize the conditions during IOP 9.

In the UTLS, vertically propagating mountain waves achieved along-track momentum flux (vertical energy flux) values varying from about zero up to $\approx$130 $kN\,m^{-1}$ ($\approx$4000 $kW\,m^{-1}$). Smith et al. (2016) classified all DEEPWAVE IOPs into weak and strong flux events, applying a threshold value of $EF_z = 4\,W\,m^{-2}$ (leg average converted to leg integrated: $EF_z \approx 1600\,kW\,m^{-1}$). As before, the transient character of the low-level forcing conditions and the wave attenuation does not allow a unique assignment of IOP 9 to one of these classes.

The flow across the rugged terrain of the Southern Alps excites a broad spectrum of gravity waves. During IOP 9, horizontally long waves of $\lambda_x \approx 200$ km were only observed during the early decelerating forcing phase (Fig. 10b), when still-strong cross-mountain winds passed over the whole SI of NZ. The observed retarded appearance of these waves in the mesosphere (Figs. 14, 19) confirms their essentially hydrostatic character and agrees with previous studies (Smith et al. 2009; Bramberger et al. 2017). Shorter waves were present in the UTLS at all times (Figs. 10a–d, 14–16). Their transient character could be observed over the Dunstan Mountains, an isolated, single ridge that is by far the highest elevation seen by the incoming flow from northwest in the vicinity of more than 40-km distance (Fig. 3). The role of the Dunstan Mountains can be compared with the Monte Rosa case of MAP on 8 November 1999. There, only the flow over the last and the highest peaks in the sequence of several ridges excited mountain waves, as the air was trapped in valleys located upstream (Smith et al. 2007). Therefore, findings were mainly based on the observation of waves over Monte Rosa. During IOP 9, waves over the Dunstan Mountains were first not observed at the stratospheric flight level (Figs. 14a,b). Only late during the maximum forcing phase part II were waves over the Dunstan Mountains detected in the lower stratosphere (Figs. 14c,d), confirming improved upper-tropospheric propagation conditions for the small-scale waves. Later, upward propagation in the upper troposphere (Figs. 15a,b) and partial wave reflection in the lower stratosphere (Figs. 15c,d) in the early decelerating forcing phase were observed. Those upward- and downward-propagating waves over the Dunstan Mountains dominated the small-scale energy and momentum fluxes. Finally, we found the significant reduction of wave activity on the basis of decreasing vertical displacements (Figs. 10b–d) and decreasing momentum and energy fluxes (Figs. 15, 16) over the Dunstan Mountains during the entire decelerating forcing phase.

The comparison of the 2D quasi-steady runs with the transient WRF run and the observations was focused on the UTLS along-track momentum fluxes. To a large extent, the quasi-steady momentum fluxes in the UTLS agree quantitatively with the transiently simulated and observed values. Agreement was found for the maximum and the mid-decelerating forcing phase, when the variability of the steady runs is considered (error bars in Fig. 11). The steady-state runs do not capture the retarded enhancement of momentum fluxes extending further into the early decelerating forcing phase in the observation of FF01 leg 2 and in the transient run. This finding encourages the hypothesis that UTLS momentum fluxes, as observed along the Mt-A-2b transect, seem to be reproducible by individual quasi-steady 2D runs, except for the retarded flux enhancement during the early decelerating forcing phase. However, this statement is only based on leg-integrated momentum fluxes. We did not investigate particular wave structures in the transient and the stationary runs, as done by Menchaca and Durran (2017) for simulations of a crossing cyclone over an isolated ridge.

6. Conclusions

The DEEPWAVE case study presented here combines in situ and remote sensing measurements to follow the deep vertical propagation of mountain waves from the troposphere to the mesosphere. The observational findings of a mountain-wave event under transient tropospheric forcing were complemented by numerical simulations covering the atmosphere up to about 33-km altitude. Among a series of transient mountain-wave events during DEEPWAVE, the analyzed IOP 9 was the only transient case of the campaign that was observed in such detail and duration, especially by the successive deployment of the two research aircraft

NSF/NCAR GV and the DLR Falcon. In this way, our study extends previous theoretical and numerical considerations of transient mountain wave events of Lott and Teitelbaum (1993a,b) and Chen et al. (2005, 2007).

Although the observed low-level forcing roughly follows the sinusoidal temporal dependence of the cross-mountain wind used in these studies, our case study reveals the importance of the time-varying propagation conditions during the period when a migrating trough and connected fronts controlled the transient forcing over NZ. With the evolving synoptic situation, the upper-tropospheric stability, the wind profile, and the tropopause strength and altitude changed and controlled the transience of the event together with the low-level forcing. In particular, the occurrence of the low-stability layer and the double jet resulted in wave attenuation and mountain wave breaking in the UTLS. In contrast, upper-stratospheric conditions changed only marginally due to the presence of a nearly steady PNJ.

During the event, maximum vertical displacements $\eta \approx 1500$ m and along-track momentum fluxes $-\mathrm{MF}_{\mathrm{track}}$, varying from around zero to $\approx 130\,\mathrm{kN\,m^{-1}}$, were observed in the UTLS. Both large- and small-scale waves contributed to these maxima during the transition from maximum to decelerating forcing. These maxima in the UTLS appeared with a phase shift of ≈ 8 h, compared to the maximum in the $\cos^2$-shaped low-level cross-mountain flow.

Small-scale waves ($\lambda_x \leq 30$ km) appeared continuously over individual orographic peaks and with large amplitudes in the troposphere. However, during the maximum forcing phase part I, their vertical propagation was limited to the troposphere due to the mentioned upper-tropospheric low-stability layer. The existence of a strong TIL suggests wave reflection and a reduction of net upward energy flux. Therefore, simulated and observed along-track momentum fluxes of small-scale waves remained small at the stratospheric flight level ($\mathrm{MF}_{\mathrm{track}} < 20\ \mathrm{kN\,m^{-1}}$). Later, when the TIL weakened, λ_{crit} decreased and small-scale wave activity increased in the lower stratosphere. There, however, a double jet associated with two vertically stacked branches of the STJ stimulated nonlinear processes such as wave breaking.

Other wave-breaking layers were observed between 15- and 25-km altitude inside the stratospheric wind minimum. As indicated by Kruse et al. (2016), the ratio of amplitudes of wave-induced velocity perturbation to the magnitude of stratospheric wind controls whether wave breaking occurs. We further found that in the case of wave breaking in the stratospheric wind minimum, upward-propagating small-scale waves seem to be reflected at this layer, explaining the observed downward-propagating waves above the tropopause.

In accordance with the decreasing low-level wind in the decelerating forcing phase, the observed short-wave along-track momentum fluxes in the UTLS diminished and achieved nearly the same small values as during the maximum forcing phase. Corresponding simulated values were higher. Wagner et al. (2017) explain this overestimation of the numerical simulations by a lack of turbulent diffusion that comes into effect when the propagation conditions also allow for the shortest waves to propagate upward.

The temporal appearance and intensity of horizontally longer waves differs from the small-scale waves during this event. The spectral analysis revealed that long waves ($\lambda_x > 30$ km) were detected only temporarily under and after the maximum in the low-level forcing. This means only the strong flow over the entire island favored their excitation. In this way, the excitation of long waves differs from the continuously excited small-scale waves. During the maximum forcing phase, long waves carried most energy and momentum into the lower stratosphere. At the transition from maximum to decelerating forcing phase, long waves with $\lambda_x > 100$ km still produce higher flux values of $\approx 80\,\mathrm{kN\,m^{-1}}$, compared to the small-scale waves. In contrast to the small-scale waves, the change of background wind and stability does not influence the vertical propagation of long waves with $\lambda_x \approx 200$ km. These waves propagated deeply upward and carried high flux values. Their longer propagation time of $\mathcal{O} \approx 12, \ldots, 15$ h calculated from the UTLS region resulted in a delayed appearance in the mesosphere. In total, the transience of increasing and decreasing mesospheric wave activity is time shifted to the low-level forcing by about 1 day.

Moreover, it was investigated whether the wave response in the UTLS can be described by a sequence of individual steady states. For this purpose, along-track momentum flux values were simulated by six 2D WRF runs initialized at different times in the course of the event. As a result, UTLS momentum fluxes seem to be reproducible by individual quasi-steady 2D runs, except for the flux enhancement during the early decelerating forcing phase. The well-satisfied Eliassen–Palm relation for the flight-level observations further suggests a quasi-steady state behavior of the nearly linear mountain waves in the UTLS (Smith et al. 2008, 2016). Indeed, parts of the wave event can be described by individual steady states. On the other hand, our results also reveal the importance of including the total transience of the event. The effect of temporally shifted wave activity in the mesosphere, compared to the UTLS, due to dispersive wave propagation cannot be

captured by quasi-steady simulations. This higher-altitude effect, including the excitation and modified propagation of various wave scales, can be considered to be another major extension to existing idealized and numerical studies of transient mountain-wave events.

Acknowledgments. Part of this research was funded by the German research initiative Role of the Middle Atmosphere in Climate (ROMIC), funded by the German Ministry of Research and Education in the project Investigation of the life cycle of gravity waves (GW-LCYCLE) and by the Deutsche Forschungsgemeinschaft (DFG) via the Project MS-GWaves (GW-TP/DO1020/9-1, PACOG/RA1400/6-1). Mesoscale simulations were performed at the Leibniz Institute for Atmospheric Physics (IAP) in Kühlungsborn, Germany. The special project HALO Mission Support System allowed the access to the ECMWF data. Gulfstream V (GV) data were provided by NCAR/EOL under sponsorship of the National Science Foundation (http://data.eol.ucar.edu/). The development of the GV AMTM was funded by the NSF Grant AGS-1061892, and its operations during the DEEPWAVE campaign by the NSF Grant AGS-1338666. We further thank the DLR facility Flight Experiments for providing the Falcon noseboom data.

APPENDIX

Wavelet Analysis

The definition of the wavelet cospectra for the vertical energy and horizontal momentum flux follows Woods and Smith (2010, 2011):

$$\widetilde{\mathrm{EF}}_{z_n}(s_j) = \Re\{\tilde{W}[p']_n(s_j)\tilde{W}^*[w']_n(s_j)\} \tag{A1}$$

and

$$\widetilde{\mathrm{MF}}_{\mathrm{track}_n}(s_j) = \Re\{\tilde{W}[u'_{\mathrm{track}}]_n(s_j)\tilde{W}^*[w']_n(s_j)\}, \tag{A2}$$

where $\tilde{W}$ is the wavelet transform of the respective quantity (u'_{track}, w', and p'), $\Re$ is the real part, and the star denotes the complex conjugate; n and j are the indices in distance and scale s, respectively. According to Liu et al. (2007), the wavelet transforms are divided by the scale parameter $s^{1/2}$; that is, they are scaled to ensure comparable spectral peaks across scales. Apart from the definition by Woods and Smith (2010, 2011), the cospectrum is further reconstructed to yield applicable physical units (factor of $\delta j \delta x^2/C_\delta$) and to be directly comparable to the leg-integrated flux values. The spatially and spectrally integrated values of the reconstructed cospectrum thus result in the leg-integrated flux. The scaled and reconstructed cospectra are finally given by

$$\mathrm{EF}_{z_n}(s_j) = \delta j \delta x^2/C_\delta \times \widetilde{\mathrm{EF}}_{z_n}(s_j)/s_j \tag{A3}$$

and

$$\mathrm{MF}_{\mathrm{track}_n}(s_j) = \overline{\rho} \times \delta j \delta x^2/C_\delta \times \widetilde{\mathrm{MF}}_{\mathrm{track}_n}(s_j)/s_j, \tag{A4}$$

with the unique reconstruction factor for the Morlet mother wavelet $C_\delta = 0.776$, the horizontal spacing δx, and the wavenumber resolution δj (Torrence and Compo 1998; Woods and Smith 2011).

To differentiate gravity waves from background noise, tests for statistical significance are applied that are based on the statistical distribution of the cospectrum. Tests are conducted at the $\alpha = 5\%$ significance level. What appears as significant according to the tests depends on the assumed background spectrum. First, the distribution of the cospectrum has to be determined: assuming stochastically independent (p' and u' are not a function of w')[2] and normal distributed [$\mathcal{N}(\mu, \sigma)$] time series, the wavelet transforms $\tilde{W}[w']_n(s_j)$, $\tilde{W}[p']_n(s_j)$, and $\tilde{W}[u']_n(s_j)$ are normal distributed as well. This is because the wavelet transform is a convolution of the time series with a scaled and translated wavelet function (Torrence and Compo 1998), and the statistical normal distribution is invariant with respect to a convolution. The cospectrum, in turn, is the real part of the product of the normal distributed wavelet transforms [Eqs. (A1) and (A2)]. According to the definition of the χ^2 distribution in Ross (2009), the cospectra are then χ^2_2 distributed with 2 degrees of freedom. With the knowledge of the distribution of the cospectra, the significant parts of, for example, the energy flux cospectrum are thus calculated by

$$\frac{\left|\widetilde{\mathrm{EF}}_{z_n}(s_j)\right| \times 2}{\sqrt{|\sigma_p^2 P_k^p \times \sigma_w^2 P_k^w|} \times Q_{\chi^2_2}(1-\alpha)} \geq 1, \tag{A5}$$

with the original wavelet cospectrum $\widetilde{\mathrm{EF}}_{z_n}(s_j)$ of Eq. (A1), the $(1-\alpha)$ quantile (cutoff value) $Q_{\chi^2_2}(1-\alpha)$ of the χ^2_2 distribution, the variance σ^2, and the normalized background spectrum P_k for each quantity. To reflect the energy distribution among the wave scales, the

[2] However, it has to be noted that p' is a function of u'. See Queney (1948): $w' = U\partial\eta/\partial x$, $u' = U\partial\eta/\partial z$, $p' = -\rho U u'$.

Markov red-noise spectrum was chosen as the background spectrum:

$$P_k = \frac{1 - \text{lag1}^2}{1 - 2\,\text{lag1} \times \cos\left(\frac{dt}{s_j \times \text{Fourier factor}}\right) + \text{lag1}^2}. \quad \text{(A6)}$$

Here, lag1 is an appropriately chosen lag-1-autocorrelation factor of the respective time series (Torrence and Compo 1998). This means the original time series is correlated with a delayed copy of itself. With a time lag of one (five), the copy would be delayed by one (five) time step(s), given by the temporal resolution of the time series (here, 1 s). A combination of a lag-1-autocorrelation with a higher lag-5-autocorrelation $[(\text{lag1} + \sqrt{\text{lag5}})/2]$ is taken for an expected gravity wave spectrum, ranging from the turbulent scale up to a few hundreds of km wavelength in order. This is done to include signals of large wavelengths (significant for higher time lags) and not to stress the signals of the smaller wavelengths (significant for smaller time lags). Equation (A5) for the calculation of significant parts of the cospectra is different from Eq. (9) in Woods and Smith (2011), especially in the fact that the latter would only expect positive $\widetilde{\text{EF}}_{z\,n}(s_j)$.

REFERENCES

Birner, T., A. Dörnbrack, and U. Schumann, 2002: How sharp is the tropopause at midlatitudes? *Geophys. Res. Lett.*, **29**, https://doi.org/10.1029/2002GL015142.

Bossert, K., and Coauthors, 2015: Momentum flux estimates accompanying multiscale gravity waves over Mount Cook, New Zealand, on 13 July 2014 during the DEEPWAVE campaign. *J. Geophys. Res. Atmos.*, **120**, 9323–9337, https://doi.org/10.1002/2015JD023197.

Bramberger, M., and Coauthors, 2017: Does strong tropospheric forcing cause large-amplitude mesospheric gravity waves? A DEEPWAVE case study. *J. Geophys. Res. Atmos.*, **122**, 11 422–11 443, https://doi.org/10.1002/2017JD027371.

Chen, C.-C., D. R. Durran, and G. J. Hakim, 2005: Mountain-wave momentum flux in an evolving synoptic-scale flow. *J. Atmos. Sci.*, **62**, 3213–3231, https://doi.org/10.1175/JAS3543.1.

——, G. J. Hakim, and D. R. Durran, 2007: Transient mountain waves and their interaction with large scales. *J. Atmos. Sci.*, **64**, 2378–2400, https://doi.org/10.1175/JAS3972.1.

Dörnbrack, A., M. Leutbecher, R. Kivi, and E. Kyrö, 1999: Mountain-wave-induced record low stratospheric temperatures above northern Scandinavia. *Tellus*, **51A**, 951–963, https://doi.org/10.3402/tellusa.v51i5.14504.

Doyle, J. D., Q. Jiang, R. B. Smith, and V. Grubišić, 2011: Three-dimensional characteristics of stratospheric mountain waves during T-REX. *Mon. Wea. Rev.*, **139**, 3–23, https://doi.org/10.1175/2010MWR3466.1.

Eckermann, S. D., and Coauthors, 2016: Dynamics of orographic gravity waves observed in the mesosphere over the Auckland Islands during the Deep Propagating Gravity Wave Experiment (DEEPWAVE). *J. Atmos. Sci.*, **73**, 3855–3876, https://doi.org/10.1175/JAS-D-16-0059.1.

Ehard, B., B. Kaifler, N. Kaifler, and M. Rapp, 2015: Evaluation of methods for gravity wave extraction from middle-atmospheric lidar temperature measurements. *Atmos. Meas. Tech.*, **8**, 4645–4655, https://doi.org/10.5194/amtd-8-9045-2015.

——, P. Achtert, A. Dörnbrack, S. Gisinger, J. Gumbel, M. Khaplanov, M. Rapp, and J. Wagner, 2016: Combination of lidar and model data for studying deep gravity wave propagation. *Mon. Wea. Rev.*, **144**, 77–98, https://doi.org/10.1175/MWR-D-14-00405.1.

Eliassen, A., and E. Palm, 1960: On the transfer of energy in stationary mountain waves. *Geofys. Publ.*, **22**, 1–23.

Fritts, D. C., and Coauthors, 2016: The Deep Propagating Gravity Wave Experiment (DEEPWAVE): An airborne and ground-based exploration of gravity wave propagation and effects from their sources throughout the lower and middle atmosphere. *Bull. Amer. Meteor. Soc.*, **97**, 425–453, https://doi.org/10.1175/BAMS-D-14-00269.1.

Giez, A., C. Mallaun, M. Zöger, A. Dörnbrack, and U. Schumann, 2017: Static pressure from aircraft trailing-cone measurements and numerical weather-prediction analysis. *J. Aircr.*, **54**, 1728–1737, https://doi.org/10.2514/1.C034084.

Gill, A. E., 1982: *Atmosphere-Ocean*. 1st ed. Academic Press, 662 pp.

Gisinger, S., and Coauthors, 2017: Atmospheric conditions during the Deep Propagating Gravity Wave Experiment (DEEPWAVE). *Mon. Wea. Rev.*, **145**, 4249–4275, https://doi.org/10.1175/MWR-D-16-0435.1.

Grubišić, V., and Coauthors, 2008: The terrain-induced rotor experiment: A field campaign overview including observational highlights. *Bull. Amer. Meteor. Soc.*, **89**, 1513–1534, https://doi.org/10.1175/2008BAMS2487.1.

Hills, M. O. G., and D. R. Durran, 2012: Nonstationary trapped lee waves generated by the passage of an isolated jet. *J. Atmos. Sci.*, **69**, 3040–3059, https://doi.org/10.1175/JAS-D-12-047.1.

Jablonowski, C., and D. L. Williamson, 2011: The pros and cons of diffusion, filters and fixers in atmospheric general circulation models. *Numerical Techniques for Global Atmospheric Models*, P. Lauritzen et al., Eds., Lecture Notes in Computational Science and Engineering Series, Vol. 80, Springer, 381–493.

Kaifler, B., N. Kaifler, B. Ehard, A. Dörnbrack, M. Rapp, and D. C. Fritts, 2015: Influences of source conditions on mountain wave penetration into the stratosphere and mesosphere. *Geophys. Res. Lett.*, **42**, 9488–9494, https://doi.org/10.1002/2015GL066465.

Keller, T. L., 1994: Implications of the hydrostatic assumption on atmospheric gravity waves. *J. Atmos. Sci.*, **51**, 1915–1929, https://doi.org/10.1175/1520-0469(1994)051<1915:IOTHAO>2.0.CO;2.

Kim, Y.-J., S. D. Eckermann, and H.-Y. Chun, 2003: An overview of the past, present and future of gravity-wave drag parametrization for numerical climate and weather prediction models. *Atmos.–Ocean*, **41**, 65–98, https://doi.org/10.3137/ao.410105.

Klemp, J. B., J. Dudhia, and A. D. Hassiotis, 2008: An upper gravity-wave absorbing layer for NWP applications. *Mon. Wea. Rev.*, **136**, 3987–4004, https://doi.org/10.1175/2008MWR2596.1.

Kruse, C. G., and R. B. Smith, 2015: Gravity wave diagnostics and characteristics in mesoscale fields. *J. Atmos. Sci.*, **72**, 4372–4392, https://doi.org/10.1175/JAS-D-15-0079.1.

——, ——, and S. D. Eckermann, 2016: The midlatitude lower-stratospheric mountain wave "valve layer." *J. Atmos. Sci.*, **73**, 5081–5100, https://doi.org/10.1175/JAS-D-16-0173.1.

Kühnlein, C., A. Dörnbrack, and M. Weissmann, 2013: High-resolution Doppler lidar observations of transient downslope

flows and rotors. *Mon. Wea. Rev.*, **141**, 3257–3272, https://doi.org/10.1175/MWR-D-12-00260.1.

Lane, T. P., M. J. Reeder, B. R. Morton, and T. L. Clark, 2000: Observations and numerical modelling of mountain waves over the Southern Alps of New Zealand. *Quart. J. Roy. Meteor. Soc.*, **126**, 2765–2788, https://doi.org/10.1002/qj.49712656909.

Liu, Y., X. San Liang, and R. H. Weisberg, 2007: Rectification of the bias in the wavelet power spectrum. *J. Atmos. Oceanic Technol.*, **24**, 2093–2102, https://doi.org/10.1175/2007JTECHO511.1.

Lott, F., and H. Teitelbaum, 1993a: Linear unsteady mountain waves. *Tellus*, **45A**, 201–220, https://doi.org/10.3402/tellusa.v45i3.14871.

——, and ——, 1993b: Topographic waves generated by a transient wind. *J. Atmos. Sci.*, **50**, 2607–2624, https://doi.org/10.1175/1520-0469(1993)050<2607:TWGBAT>2.0.CO;2.

Martin, A., and F. Lott, 2007: Synoptic responses to mountain gravity waves encountering directional critical levels. *J. Atmos. Sci.*, **64**, 828–848, https://doi.org/10.1175/JAS3873.1.

Menchaca, M. Q., and D. R. Durran, 2017: Mountain waves, downslope winds, and low-level blocking forced by a mid-latitude cyclone encountering an isolated ridge. *J. Atmos. Sci.*, **74**, 617–639, https://doi.org/10.1175/JAS-D-16-0092.1.

Pautet, P.-D., M. J. Taylor, W. R. Pendleton Jr, Y. Zhao, T. Yuan, R. Esplin, and D. McLain, 2014: Advanced mesospheric temperature mapper for high-latitude airglow studies. *Appl. Opt.*, **53**, 5934–5943, https://doi.org/10.1364/AO.53.005934.

——, and Coauthors, 2016: Large-amplitude mesospheric response to an orographic wave generated over the Southern Ocean Auckland Islands (50.7°S) during the DEEPWAVE project. *J. Geophys. Res. Atmos.*, **121**, 1431–1441, https://doi.org/10.1002/2015JD024336.

Queney, P., 1948: The problem of air flow over mountains: A summary of theoretical results. *Bull. Amer. Meteor. Soc.*, **29**, 16–26.

Reeder, M. J., N. Adams, and T. P. Lane, 1999: Radiosonde observations of partially trapped lee waves over Tasmania, Australia. *J. Geophys. Res.*, **104**, 16 719–16 727, https://doi.org/10.1029/1999JD900038.

Ross, S. M., Ed., 2009: *Introduction to Probability and Statistics for Engineers and Scientists*. 4th ed. Academic Press, 664 pp.

Rotering, H., 2011: Falcon 20-E5 trailing cone validation. German Aerospace Center, Institute of Flight Systems Rep. IB 111-2011/28, 46 pp.

Scorer, R. S., 1949: Theory of waves in the lee of mountains. *Quart. J. Roy. Meteor. Soc.*, **75**, 41–56, https://doi.org/10.1002/qj.49707532308.

Skamarock, W. C., and J. B. Klemp, 2008: A time-split nonhydrostatic atmospheric model for weather research and forecasting applications. *J. Comput. Phys.*, **227**, 3465–3485, https://doi.org/10.1016/j.jcp.2007.01.037.

——, and Coauthors, 2008: A description of the Advanced Research WRF version 3. NCAR Tech. Note NCAR/TN-475+STR, 113 pp., https://doi.org/10.5065/D68S4MVH.

Smith, R. B., 1979: The influence of the mountains on the atmosphere. *Advances in Geophysics*, Vol. 21, Academic Press, 87–230, https://doi.org/10.1016/S0065-2687(08)60262-9.

——, and C. G. Kruse, 2017: Broad-spectrum mountain waves. *J. Atmos. Sci.*, **74**, 1381–1402, https://doi.org/10.1175/JAS-D-16-0297.1.

——, J. D. Doyle, Q. Jiang, and S. A. Smith, 2007: Alpine gravity waves: Lessons from MAP regarding mountain wave generation and breaking. *Quart. J. Roy. Meteor. Soc.*, **133**, 917–936, https://doi.org/10.1002/qj.103.

——, B. K. Woods, J. Jensen, W. A. Cooper, J. D. Doyle, Q. Jiang, and V. Grubišić, 2008: Mountain waves entering the stratosphere. *J. Atmos. Sci.*, **65**, 2543–2562, https://doi.org/10.1175/2007JAS2598.1.

——, and Coauthors, 2016: Stratospheric gravity wave fluxes and scales during DEEPWAVE. *J. Atmos. Sci.*, **73**, 2851–2869, https://doi.org/10.1175/JAS-D-15-0324.1.

Smith, S., J. Baumgardner, and M. Mendillo, 2009: Evidence of mesospheric gravity-waves generated by orographic forcing in the troposphere. *Geophys. Res. Lett.*, **36**, L08807, https://doi.org/10.1029/2008GL036936.

Snively, J. B., V. P. Pasko, and M. J. Taylor, 2010: OH and OI airglow layer modulation by ducted short-period gravity waves: Effects of trapping altitude. *J. Geophys. Res.*, **115**, A11311, https://doi.org/10.1029/2009JA015236.

Strauss, L., S. Serafin, and V. Grubišić, 2016: Atmospheric rotors and severe turbulence in a long deep valley. *J. Atmos. Sci.*, **73**, 1481–1506, https://doi.org/10.1175/JAS-D-15-0192.1.

Teixeira, M. A. C., 2014: The physics of orographic gravity wave drag. *Front. Phys.*, **2**, 43, https://doi.org/10.3389/fphy.2014.00043.

Torrence, C., and G. P. Compo, 1998: A practical guide to wavelet analysis. *Bull. Amer. Meteor. Soc.*, **79**, 61–78, https://doi.org/10.1175/1520-0477(1998)079<0061:APGTWA>2.0.CO;2.

Wagner, J., and Coauthors, 2017: Observed versus simulated mountain waves over Scandinavia—Improvement of vertical winds, energy and momentum fluxes by enhanced model resolution? *Atmos. Chem. Phys.*, **17**, 4031–4052, https://doi.org/10.5194/acp-17-4031-2017.

Wallace, L., 1962: The OH nightglow emission. *J. Atmos. Sci.*, **19**, 1–16, https://doi.org/10.1175/1520-0469(1962)019<0001:TONE>2.0.CO;2.

Woods, B. K., and R. B. Smith, 2010: Energy flux and wavelet diagnostics of secondary mountain waves. *J. Atmos. Sci.*, **67**, 3721–3738, https://doi.org/10.1175/2009JAS3285.1.

——, and ——, 2011: Short-wave signatures of stratospheric mountain wave breaking. *J. Atmos. Sci.*, **68**, 635–656, https://doi.org/10.1175/2010JAS3634.1.